Ceramics International 46 (2020) 2987–3001

Contents lists available at ScienceDirect

Ceramics International

journal homepage: www.elsevier.com/locate/ceramint

# Insights on the mechanism of solid state reaction between $TiO_2$ and $BaCO_3$ to produce $BaTiO_3$ powders: The role of calcination, milling, and mixing solvent

J.L. Clabel H[a,*], Iram T. Awan[a], Alexandre H. Pinto[b], I.C. Nogueira[c], V.D.N. Bezzon[d], E.R. Leite[e], Debora T. Balogh[a], Valmor R. Mastelaro[a], S.O. Ferreira[f], E. Marega Jr.[a]

[a] São Carlos Institute of Physics, University of São Paulo, 13560-970, São Carlos, SP, Brazil
[b] Chemistry and Biochemistry Department, Manhattan College, Riverdale, NY, 10471, USA
[c] Department of Physics, Federal University of Amazonas, 69077-000, Manaus, AM, Brazil
[d] Department of Physics, Aeronautics Institute of Technology, 12228-970, São Jose Dos Campos, SP, Brazil
[e] Department of Chemistry, Federal University of São Carlos, 13565-905, São Carlos, SP, Brazil
[f] Department of Physics, Federal University of Viçosa, 36570-90l, Viçosa, MG, Brazil

A B S T R A C T

Barium titanate ($BaTiO_3$) is well-known for its variety of macroscopic properties, however, the mechanism of formation of this oxide in microscale remains poorly understood. We prepared the $BaTiO_3$ nanoparticles and studied them as a function of milling time and temperature. A systematic study was performed to understand the reaction mechanism of undissociated and dissociated 2-propanol molecules on $TiO_2$ and $BaCO_3$ particles. Structural evolution and thermal decomposition of surface particles were carried out and studied by X-ray diffraction, scanning electron microscopy (SEM) and Fourier transform infrared (FTIR) spectroscopy analysis. Structural parameters refined by Rietveld analysis using X-ray diffraction data revealed a tetragonal structure with P4/mm space group, which was due to the dependence of functional groups on the milling time and thermal treatment. The divergence of tetragonality as a function of thermal treatment was identified for particles of size < 400 nm, which probably happened due to surface defects which decreased in low temperature of about 1000 °C. Particle sizes precursors decreased as a function of the milling time from 18 μm (2 h milling) to 1.2 μm (24 h of milling). While by increasing the thermal treatment of samples from 1000 °C to 1100 °C the particles size increased, respectively, 0.24 μm and 0.36 μm. The effect of the particle size of $TiO_2$ plays an important role in the reaction kinetics of the formation of $BaTiO_3$. Our results suggest that the reaction proceeds through a mechanism in which the intermediate processes of $TiO_2$, $BaCO_3$ and dissociation of $BaCO_3$ are trapped by the dissociated and undissociated 2-propanol molecules, which resulted in depletion of 2-propanol-related functional groups in the $BaTiO_3$ particle surface at higher temperature.

## 1. Introduction

Barium titanate ($BaTiO_3$) has attracted considerable attention due to its unique physical and chemical properties which can be used in applications such as ferroelectric ceramics [1], catalysis of organic reactions [2,3], multiferroic materials [4–6] and optical devices [7]. The efficiency of functionality of such materials is based on the method of synthesis which is accompanied by the intrinsic reaction mechanism. Solid state reaction method (SSRM) is a synthetic process to prepare $BaTiO_3$, frequently used due to the fact that it is a quick and a low-cost method, that can be performed in solutions suspended in a ball milling. Considering $BaCO_3$ and $TiO_2$, respectively, as the sources of barium and titanium during the SSRM. $BaCO_3$ has an orthorrombic structure. Contrastingly, $TiO_2$ has different polymorphic structures, for instance, rutile, anatase, and brookite, which have distinctive optical properties. Consequently, the photocatalytic activity of $BaTiO_3$ product is likely to be dependent on the $TiO_2$ polymorph and also the solvent used to promote the solid state reaction. Additionally, the induced photocatalytic activity of $TiO_2$ gives rise to surface defects which seems to be very correlated to the increase of the specific surface area [8–11].

Early studies on the production process were focused on the reaction kinetics after the mixing process [12]. The reaction kinetics include very complex reactions between intermediates, until the formation of crystalline $BaTiO_3$ structure takes place. Different post mixture reaction conditions, such as: thermal treatment, heating/cooling rate, time of thermal treatment and heating steps were used to study the crystallization and phase stabilization. Reaction mechanism of the mixture between reactant molecules and the solvent used is poorly studied, as a function of different milling times. In view of this fact, the present study includes very complex and sophisticated reactions that cannot be analyzed without a proposed mechanism.

Main objectives of the study are: to propose reaction mechanisms

* Corresponding author.
*E-mail address:* jclabel@ifsc.usp.br (J.L. Clabel H).

https://doi.org/10.1016/j.ceramint.2019.09.296
Received 25 June 2019; Received in revised form 16 September 2019; Accepted 30 September 2019
Available online 01 October 2019

through investigating the adsorption of functional groups, to understand the extent of dissociation of 2-propanol on the $TiO_2$ and $BaCO_3$ surface, and how pre and post thermal treatments affect the removal of surface-bound functional groups. In order to understand and minimize the possible risks of organic solvents, and to optimize the synthesis process, the functional groups produced from the adsorption of dissociated propanol, and its intermediate reactions, were studied. FTIR spectroscopy and powder X-ray diffraction were used as complementary techniques. The first one can identify both modifications in vibrational absorption and reaction of intermediates, while the second is the most commonly applied tool to provide extensive information on the quantification of the amount of crystalline phase and structural changes.

## 2. Experimental section

Barium Titanate powder was synthesized by the conventional solid-state reaction method (SSRM). $BaTiO_3$ ceramic powders were made by combining precursors barium carbonate (99.98%) and titanium dioxide (≥99%) purchased from Sigma Aldrich. 2-propanol (99.5%), purchased from Synth, was used as a solvent. The precursors were weighed according to the required stoichiometric mole ratios to yield $BaTiO_3$ (in 1:1 relation). $BaCO_3 = 1.27g$ $(6.4 \times 10^{-3}\,mol)$ and $TiO_2 = 0.51g$ $(6.4 \times 10^{-3}\,mol)$ were mixed in a ball mill with 2-propanol (4.5 mL) as solvent and zirconium oxide balls (0.5 mm) as the milling medium, see Fig. 1. As different milling times determine the size of the particles, we chose three different time spans of 2, 12 and 24 h for milling at 40 rpm and hence after thermal treatment got $BaTiO_3$ in three different average particle sizes. Afterwards the powders were calcined at the temperatures of 1000 °C and 1100 °C, to verify the effect of calcination on the particle size and on the crystalline phase of the $BaTiO_3$.

Particle size distribution in the samples was analyzed using a SediGraph 5100 (Micromeritics Instrument Co., USA), which is based on Stokes law and low energy X-ray absorption. X-ray diffraction was performed on a Rigaku Dmax 2500 PC diffractometer of CuKα radiation in an angular range between 10° and 75° with 2° $min^{-1}$ of scanning velocity and 0.02° step size. The Rietveld Method, for refinement and quantitative phase analysis was performed by TOPAS Academic program using the Fundamental Parameters approach implemented in this program. The structure models used in the refinement have been indexed in the Inorganic Crystal Structure Database (ICSD). All lattice cell parameters were refined and in all the refinements the background was adjusted using a Chebyshev polynomial function with five terms. The quality of the refinements was checked by the agreement factors (weighted pattern R-factor $R_{wp}$, expected R-factor $R_{exp}$, Bragg R factor $R_{Bragg}$ or $R_p$ and goodness-of-fit $\chi^2$) and the graphical adjustment. A SEM instrument (Model XL, Philips, Japan) operated at 25 kV determined the morphology and composition of BT powders. The milling, pH, calcination, and resulting particle size of the $BaTiO_3$ (BT) samples prepared in this study are shown in Table 1.

**Table 1**
Conditions for formation of the powder $BaTiO_3$ and particle size.

| Powder | Milling (hours) | pH of solution after milling process | Calcination (°C) | Particles size (μm) |
|---|---|---|---|---|
| BT1 | 2 | 7.1 | r.t. | 18 |
| BT2 | 12 | 6.3 | r.t. | 14 |
| BT3 | 24 | 4.2 | r.t. | 1,2 |
| BT1-1 | 2 | – | 1000 | 0.99 |
| BT1-2 | 2 | – | 1100 | 1.23 |
| BT2-1 | 12 | – | 1000 | 0.37 |
| BT2-2 | 12 | – | 1100 | 0.44 |
| BT3-1 | 24 | – | 1000 | 0.24 |
| BT3-2 | 24 | – | 1100 | 0.36 |

* pH of the solution (pH value of 2-propanol is 7.4) r.t. = room temperature.

The concept of pH is applied to aqueous solutions based on the autoionization of water which lead to the formation of cations (positively-charged ions) and anions (negatively-charged ions). However, it can also be applied to the non-aqueous solutions because the proton activity term is applicable to organic medium as well as its applicable to water. In such sense, experiments with precursors barium carbonate and titanium dioxide were conducted in a pH range of 1 to 14 at room temperature, obtained by adding the appropriate amount of solvent of 2-propanol. The value of pH of 2-propanol was considered as reference (pH = 7.4). The pH of solution changed after the process of milling, where measurements were performed in different times, see Table 1.

Infrared (IR) measurements were taken in a Fourier transform infrared (FTIR) spectrometer Nicolet Nexus 470, in transmittance mode. All spectra were collected under ambient conditions. The spectra were recorded in the range of 4000 to 400 $cm^{-1}$ with a resolution of 4 $cm^{-1}$.

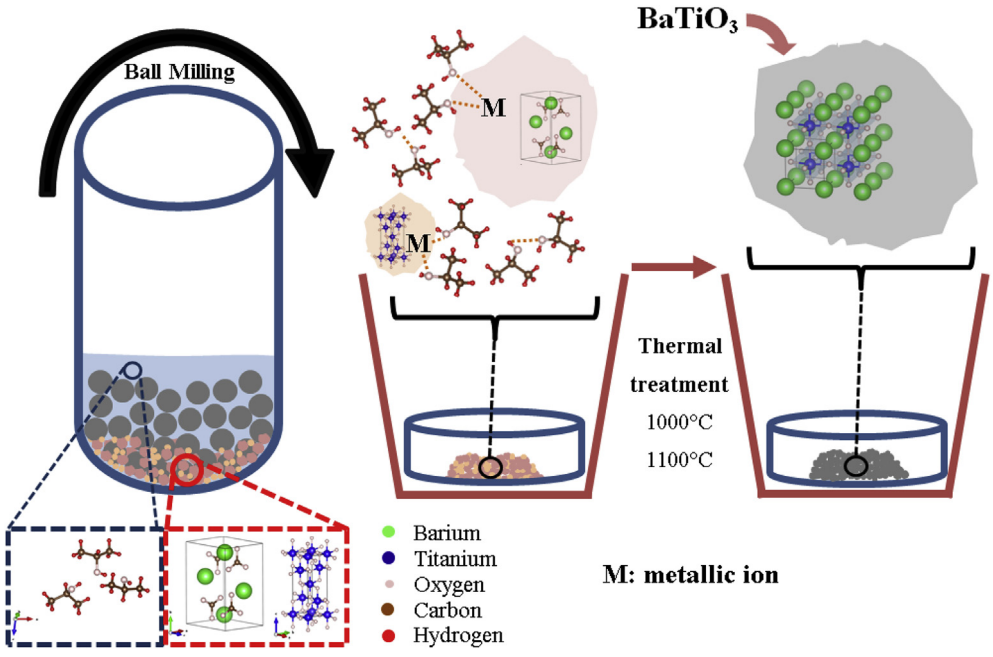


**Fig. 1.** Schematic views of the synthesis process by solid state reaction to prepare powders of $BaTiO_3$.

The BT samples were finely ground, mixed thoroughly with potassium bromide (KBr:1% sample) in an agate mortar, pressed into pellets, and desiccated prior to the analysis. Utilizing proper data analysis tools, the correlation of FT-IR spectra with functional groups can be achieved, as will be shown later. In this sense, the following steps were followed: 1) Second derivative of spectra were obtained to identify the possible number of the frequencies positions of the underlying spectral components. The frequencies of the band centers thus measured were used as initial input parameters for the deconvolution procedure (band-fitting), 2) Deconvolution was carried out by using an optimal fitting function to define the individual components and peak parameters such as, frequency positions, area under the band, peak intensity and full width at half maximum (FWHM). In our analysis, the mixing of Gaussian and Lorentzian function achieved the best fitting of the spectra [13]. The deconvolution of the function was processed using the software "Peakfit" v. 4.12 (Jandel, Scientific Software), which enabled the selection of the type of the fitting function and also allowed to fix or vary some specific parameters accordingly.

## 3. Results and discussion

### 3.1. Structural and microstructural properties

Fig. 2 shows the X-ray diffraction (XRD) results. The diffraction peaks of the samples BT1, BT2, and BT3 were identified as a mixture of $BaCO_3$ (ISCD file number 56100) [14] and anatase $TiO_2$ (ICSD file number 9852) [15], see Fig. 2(a). Anatase, observed as the crystalline phase for $TiO_2$ is an expected fact, since it is the crystalline phase for the $TiO_2$ that is used as a reagent, as confirmed by the XRD (see Figure R1 in Supporting Information). During the process of calcination the anatase $TiO_2$, contributes favorably to the surface reactions than for example, the rutile [16]. Furthermore, anatase has a larger band gap than rutile $TiO_2$, although this influences on the band gap of $BaTiO_3$, reducing the light that can be absorbed, it may also raise the valence band maximum to higher energy levels. These changes can increase the generation of electron-hole and facilitates the electron transfer from the valence band. Such factors are important in the performance of the optical properties of $BaTiO_3$. As these samples were not subjected to any calcination step, hence, all the peaks presented for all the three samples could be explained based on the mixture of $BaCO_3$–$TiO_2$, which showed that the thermal treatment is a necessary step in the formation of $BaTiO_3$. For the BT samples subjected to calcination (samples from BT1-1 to BT3-2 in Table 1), single phase $BaTiO_3$ was obtained for the samples whose calcination was carried out for at least 12 h (samples BT1-2, BT2-2 and BT3-2). For the samples BT1-1 and BT2-1, which were subjected to calcination times as short as 2 h, mixtures of $BaCO_3$ and $TiO_2$ were obtained, as shown in Fig. 2(b).

The Rietveld refinements of BT powder, as shown in Fig. 3, indicates an adequate adjustment between observed and calculated profiles. The structure refinement data revealed a tetragonal symmetry with space group P4/mm according to the standard ICSD number 67519 [17], for the thermally treated BT samples.

To highlight the evolution of the crystal structure which was accompanied by the distortion of the tetragonality with milling time, the XRD patterns from 44.0° to 46.0° are shown in the inset in Fig. 3. The splitting of the (002) and (200) X-ray diffraction peak is an indicative of the tetragonality (c/a), and an indirect method to measure the lattice parameters from the **c** and **a** axes.

Splitting of the (002) and (200) peaks can be observed, which becomes distinct with the increase of temperature. Two contrary effects in the tetragonality were observed when the temperature increased; 1) at low temperature, the splitting of peaks decreased with the increase of the milling time which lead to a significant decrease in tetragonality, 2) at high temperature, the splitting of peaks gradually increased with the increase of the milling time that lead to increased tetragonality.

The structural parameters for thermally treated BT samples

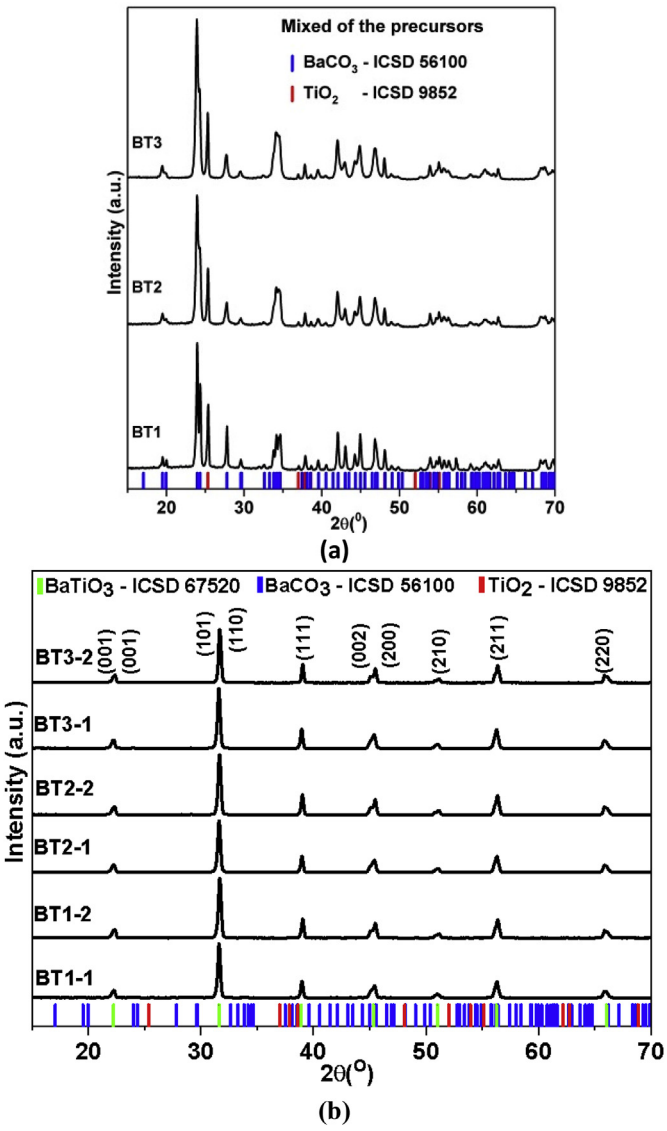


**Fig. 2.** X-ray diffraction patterns for different samples (mixtures of $TiO_2$ and $BaCO_3$) (a) before thermal treatment, (b) after thermal treatment.

obtained through refinement along with the deviations of the statistical parameters given by TOPAS software are shown in Table 2.

The VESTA software [18] allowed the simulation of the structure of the powdered BT, position of the Ba, Ti and O atoms and measurement of distortion octahedral of BT; as shown in Fig. 4(a). The result shows changes in the separation distance between the Ba atoms, for powdered BT at different temperatures consequently a distorted octahedral was observed as shown in Fig. 4(b).

Likewise, for each milling time, the tetragonality significantly increased with increase in temperature, as shown by the dashed lines in Fig. 5(a). The correlation of the milling time with particle size is linear, as shown in Fig. 5(b). In this sense, it is also known that the tetragonality depends on the particle size as referred in the literature, where smaller distortions are expected in smaller particles [19,20]. The increase in the milling time induces a decrease in the particle size, in this sense the tetragonality as a function of particle size was verified from Fig. 5(c). It is interesting to note a strong contribution to the tetragonality when the particle size is reduced. Fig. 5(b) showed a clear divergence in the curves for thermal treatment at 1000 °C and 1100 °C when the particle size is < 450 nm. The contribution to high tetragonality happened with the thermal treatment of 1100 °C, in contrast a low tetragonality was observed for the treatment of 1000 °C. The

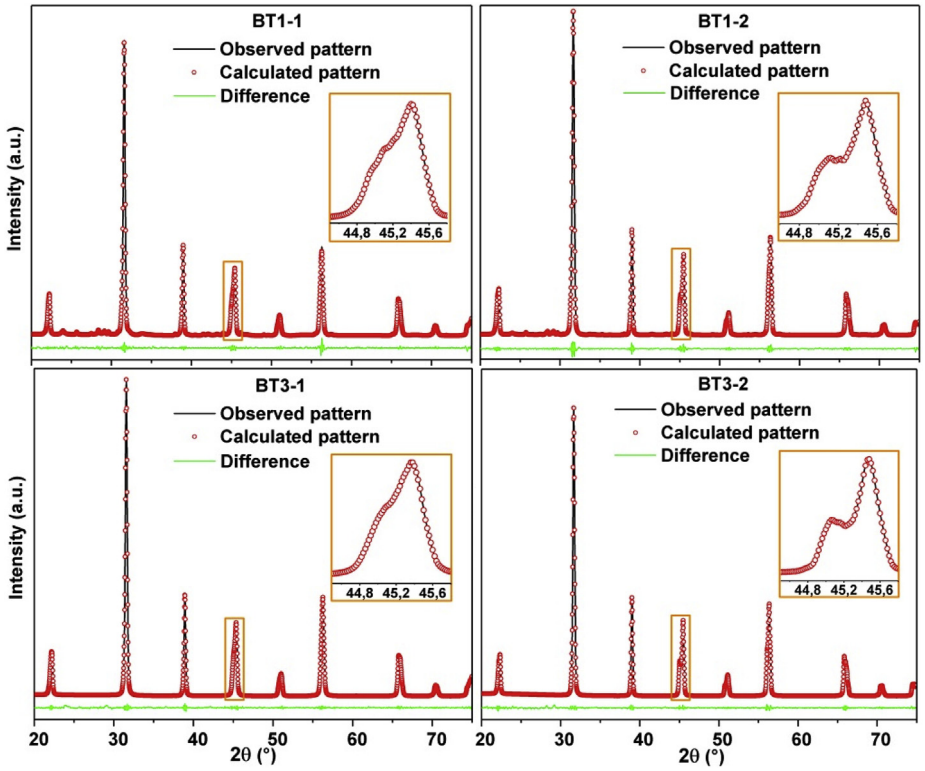


**Fig. 3.** Rietveld plots for different $BaTiO_3$ samples, after thermal treatment. The amplification of X-ray diffraction profile from 44 – 46 °C in 2θ.

**Table 2**
Refined structural parameters and respective agreement factors of the refinement to the $BaTiO_3$ samples.

| Crystallographic data | Space group | Volume (Å$^3$) | a, b (Å) | c (Å) | $R_{Bragg}$ (%) | $R_{wp}$ (%) | $R_{exp}$ (%) | $\chi^2$ |
|---|---|---|---|---|---|---|---|---|
| BT1-1 | P4/mm | 64.390(4) | 3.99899(9) | 4.02642(1) | 3.83 | 15.92 | 11.48 | 1.38 |
| BT1-2 | P4/mm | 64.390(6) | 3.99746(2) | 4.02950(2) | 3.05 | 15.10 | 11.61 | 1.30 |
| BT2-1 | P4/mm | 64.394(5) | 3.99923(1) | 4.02616(2) | 5.10 | 11.83 | 11.72 | 1.01 |
| BT2-2 | P4/mm | 64.364(5) | 3.99685(1) | 4.02905(1) | 3.53 | 11.88 | 11.22 | 1.06 |
| BT3-1 | P4/mm | 64.391(5) | 3.99898(1) | 4.02544(1) | 3.53 | 11.48 | 11.28 | 1.02 |
| BT3-2 | P4/mm | 64.394(5) | 3.99744(1) | 4.02965(1) | 5.12 | 13.08 | 12.11 | 1.08 |

maximum and minimum tetragonality at the thermal treatment of 1000 °C is observed as 1.007, with particle size of 0.99 μm and 1.006 with the particle size of 0.24 μm, respectively. Contrarily, the maximum and minimum tetragonality at the treatment of 1100 °C is observed to be 1.008 with the particle size of 0.36 μm, and 1.008 with the particle size of 1.23 μm, respectively. Hence, increase in the temperature from 1000 to 1100 °C, is the reason behind such divergence. According to our results we hypothesize that in addition to the particle size, thermal temperature is another important factor which brings divergence in tetragonality. The increase in temperature helps to remove the surface chemical defects (as will be shown in the measurement of FTIR), contributing to the increase in tetragonality. According to the literature [21,22], when the particle size of BT is smaller than 0.4 μm, the tetragonality decrease drastically. By Sakabe et al. [23] and Leonel et al. [24], the maximum tetragonality for the samples thermally treated at 1000 and 1100 °C was observed as 1.008 and 1.004, respectively. These

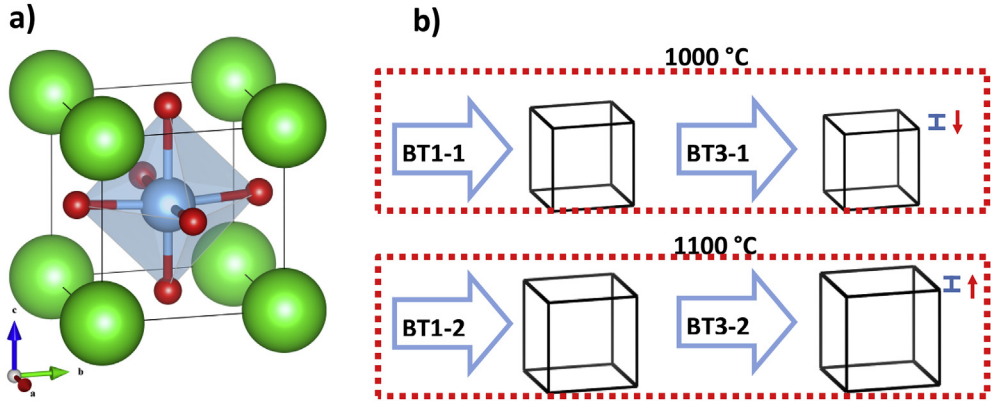


**Fig. 4.** Structure of $BaTiO_3$ from VESTA software: a) Coordination octahedral of the $BaTiO_3$, b) Variation of structure with the increasing of thermal treatment. Green (Barium atom), red (oxygen atom) and celeste (titanium atom). (For interpretation of the references to colour in this figure legend, the reader is referred to the Web version of this article.)

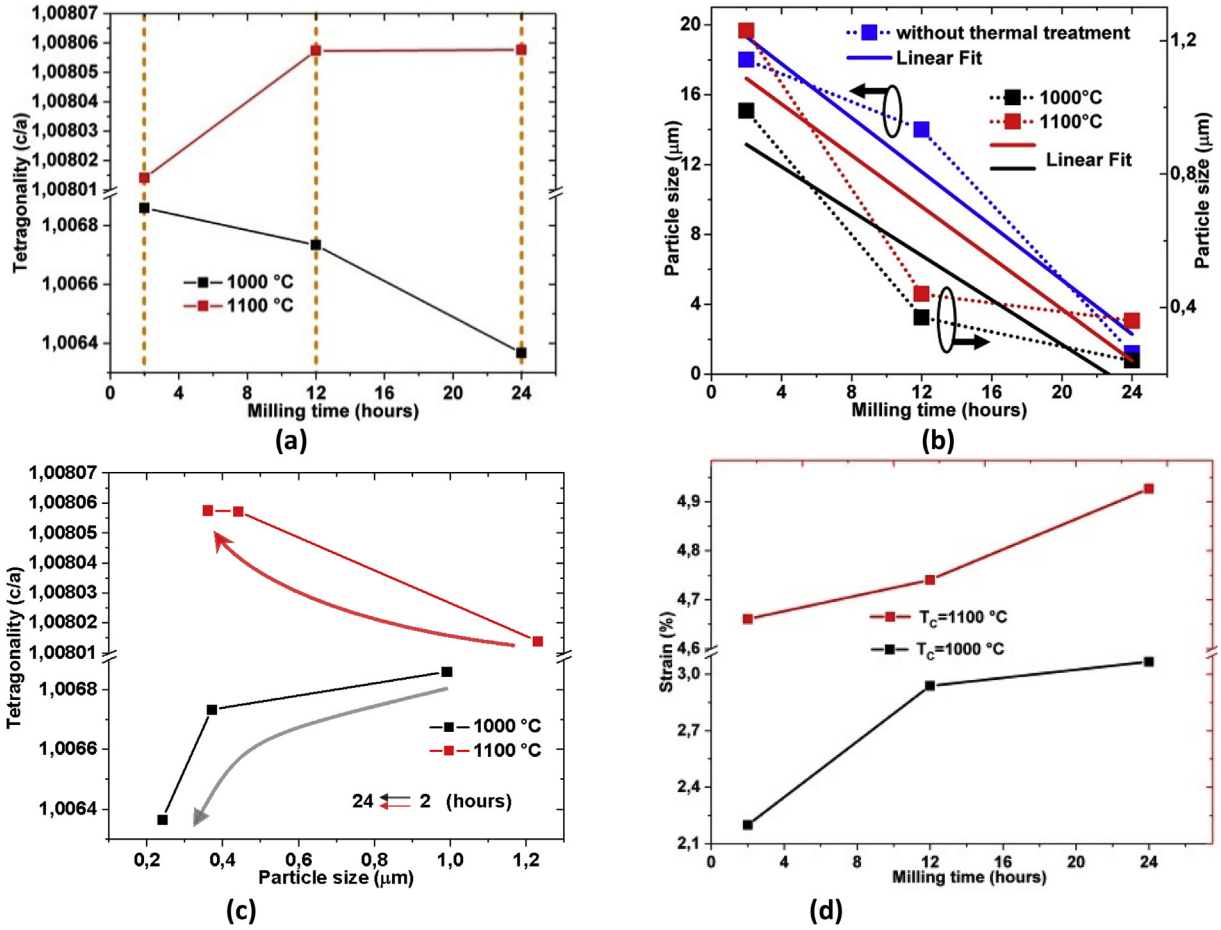


**Fig. 5.** (a) Tetragonality as a function of milling times, (b) Particle size as a function of milling time, (c) Tetragonality as a function of particle size, and (d) shows Strain as a function of milling time.

values are lower than those reported in the present study. On the other hand, the results from Kwon and Yoon [25] showed similar value of tetragonality of 1.0105 for the samples that were thermally treated between 950 and 1050 °C and presented particle size of around 320 nm. This is in contrast with our results, where an increase in the particle size was found with significant variation in tetragonality as the temperature was increased.

The accumulation of stresses in the BT lattice due to the milling process leads to the distortion of the lattice structure and to the formation of the other surface defects (such as oxygen vacancies, surface states and $OH^-$ defects), which results in further accumulation of stress in the particles. The stress in the particle depends on the presence of strain, which can be determined qualitatively by means of the Willianson-Hall equation. The dependence of the strain on the milling time of 2, 12 and 24 h for two different temperatures of 1000 °C and 1100 °C is shown in Fig. 5(d). Differences in line broadening are associated with the particle size and lattice distortion effects generated due to the strain. The strain gradually increased with the milling time for both thermally treated samples at 1000 and 1100 °C, with the latter being more significant in this regard. Ahamad et al. [26], have also reported the increase in the lattice strain as a result of less dissolution of alloying elements and reinforcement in the matrix at longer milling times. Therefore, the tetragonality gets affected more due to the thermal treatment than the particle size lower than 450 nm. The unexpected dependence is based on the contributions of chemical defects. The non-stoichiometric changes produced by the oxygen exchange with the atmosphere on the surface of particle (chemical defects), as well as its particular kinetics at elevated temperatures can be main responsible for the strain along **c** and **a** axes in the thermally treated BT samples, as affirmed by Xinhua Zhu et al. [27].

The comparison between the results for the powders that were not calcined i.e. BT1, BT2 and BT3 showed that designated ball milling contributes to the reduction in the particle sizes and to the accumulation of the stress due to the induced severe plastic deformation of the particles. According to Rouholah [16] and Pavlovic et al. [28], short milling time of 0.5 h has no significant effect on the morphology of powders except that it results in the partial deformation of the particles. However, for a milling time of above 2 h, the particles experience plastic deformation due to the high impact of collision of the balls. Such deformation leads to powders with ultrafine particles, lattice defects and dislocations in particular. The milling process in both papers was carried out in a planetary ball mill and not in a jar mill, as carried out in our work. The stress close to the surface of the particles is observed high which decreases continuously with an increase in the depth beneath the surface [29]. The stress distribution in the surface region could depend on the rpm speed, milling time and the solvent used. Shiratori et al. [30] hypothesized that occurrence of defect particles or fractures due to the stress, easily induce connection breakings and impurities at the interface within the large particles. In addition to the stress caused by the mechanical process, a further contribution is associated to the thermal process, see Fig. 5(d). Likewise, a slight variation on the degree of crystallinity and particle size is shown after the thermal treatment, especially for the BT powder treated at high temperature (1100 °C). This variation is probably due to the reason that milling time and thermal treatment caused alterations both in the lattice parameter as well as in the cell volume of the samples (see Table 2).

The microstructure and analyses of the average size distribution of the particles of $BaTiO_3$ powders were investigated by SEM and light

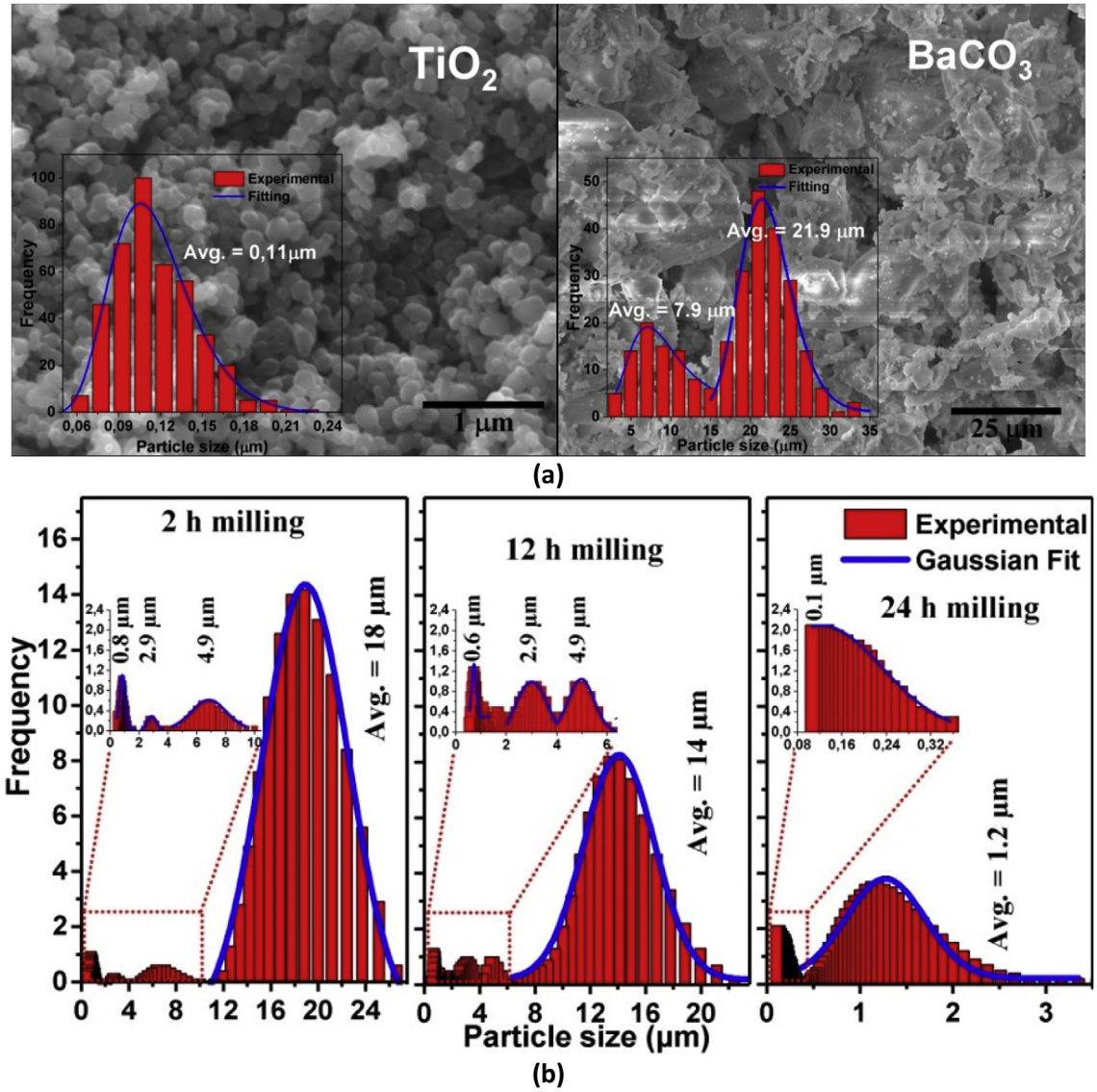


**Fig. 6.** (a) SEM images and particle size distribution of $TiO_2$ (left) and $BaCO_3$ (right) initial precursors, (b) Particle size distribution histogram of the particles resulting from the mixing of $TiO_2$ and $BaCO_3$ for different milling times.

scattering technique, respectively (see Figs. 6 and 7). The starting precursors $BaCO_3$ and $TiO_2$ presented bimodal and unimodal particle sizes of ~7.9/~21.9 and ~0.11 μm, respectively, see Fig. 6(a). The larger particle sizes can be easily broken to smaller sizes with the increase in the period of milling time (from 2, 12 and 24 h), for mixing the precursor powders, as shown in the morphologies in Fig. 6(b). A similar phenomenon was reported with barium titanate particles when fine $TiO_2$ powders were mixed with $BaCO_3$ [31–34]. The change in the SEM images can be evidenced in the particle size distribution, which was examined using Micromeritics Sedigraph 5100, as a function of milling time and after thermal treatment at different temperatures, as shown in each histogram present in the insets in Fig. 6(b). The insets of Fig. 6(b), leads to several observations: (1) samples mixed for different milling times tend to show a multimodal or bimodal size distribution, where the smaller particles are formed with the increase in milling time. In case of sample with 2 h of milling, a multimodal distribution with average particle size of around 18, 4.9, 2.9 and 0.8 μm is observed, while the samples with 12 h of milling exhibited a decreased average particle size of around 14, 4.9, 2.9 and 0.6 μm. With the increase of milling time the large value of peak intensity shifted to smaller value. In addition, it also induced a slight increase in the frequency of particles with average sizes of 4.9, 2.9 and 0.6 μm, which happened as a consequence of the breaking of the particles due to the prolonged milling. For milling time of 24 h, a significant decrease in the peak intensity is observed with the appearance of a bimodal size distribution with average particle sizes of 0.1 and 1.2 μm, respectively.

From the particle size distribution results obtained at variable milling times and without thermal treatment, we observed that particle size of $TiO_2$ is less sensitive to reduction than that of $BaCO_3$. This can be explained as follows; due to the size difference of $TiO_2$(0.11 μm) significantly lower than $BaCO_3$(7.9 and 21.9 μm), see Fig. 6(a), the $TiO_2$ particles occupy the interstitial volumes, generated by the $BaCO_3$ particles, thus allowing more interaction between the particles of $BaCO_3$ [35–37]. As the milling time increased the probability of agglomeration of $TiO_2$ particles in the interstitial volumes decreased, since the interstitial volumes became unable to accommodate multiple $TiO_2$ particles. Additionally, in shorter milling time (2 h), the packing of $TiO_2$ particles in the interstitial spaces can also undergo agglomeration, which lowers the scattering efficiency of each $TiO_2$ particle. Contrarily, in larger milling times (12 or 24 h), more uniform dispersion of the $TiO_2$ particles is allowed which reduces the effect of agglomeration. In general terms, the increase in the milling times leads to a decrease in the

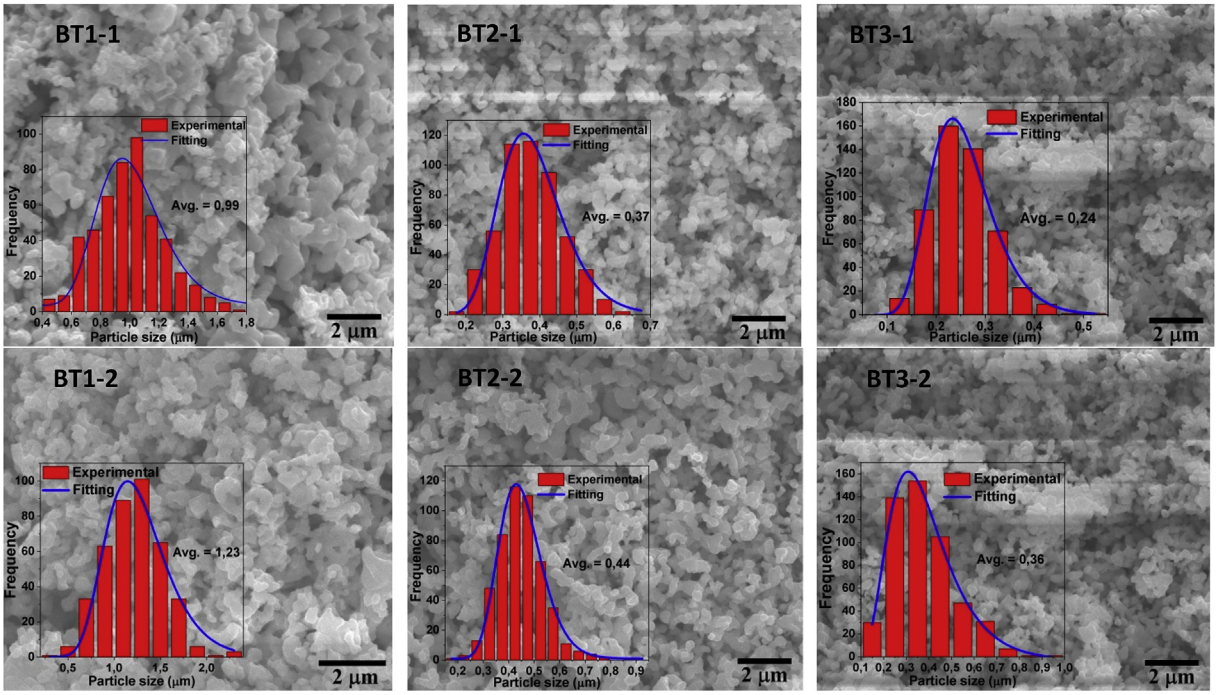


**Fig. 7.** SEM micrographs and distribution of the particle sizes of barium titanate powders after milling of 2, 12 and 24 h and thermally treating at 1000° and 1100 °C.

amount of larger particles, and consequently, increases the amount of smaller particles.

Considering the particle size of the precursors $TiO_2$ (0.11 μm) and $BaCO_3$ (21.9 μm) and after different grinding times (see Fig. 6), it was also observed that with the increase in the temperature (from 1000 °C to 1100 °C), the effect of the particle size of $TiO_2$ plays an important role in the reaction kinetics of the formation of $BaTiO_3$ (see Fig. 7). Since the formation of $BaTiO_3$ occurs on the surface of $TiO_2$, it implies that it is independent of the size of the $BaCO_3$ [38,39]. Homogeneous particles with low agglomeration can be obtained after thermal treatment of such powders, as shown in Fig. 7. At the temperature of 1000 and 1100 °C, the particle size is homogeneous and therefore shows a monomodal distribution, as shown in the inset of Fig. 7. In these conditions, higher temperatures accelerate the initial stage of the reaction but leads to coarser and more-agglomerated powders, which are different than less agglomerated $BaTiO_3$ powders. A gradual increase in the average particle size from 0.99 to 1.23 μm in the samples BT1-1 and BT1-2 is observed after an increase in the treatment temperature. Similar behavior, although with small average particle size, is noticed in going from sample BT2-1 to BT2-2 and BT3-1 to BT3-2 with a size variation from 0.37 to 0.44 μm and 0.24 to 0.36 μm, respectively. In this work, coarsening of $BaTiO_3$ is definitively established in the different stages (milling times), which is mainly dominated by the particle size of $TiO_2$. According to a previous report, the solid-state reaction kinetics between $BaCO_3$ and $TiO_2$, for the formation of $BaTiO_3$ occurs at the boundary of the interfaces $BaCO_3/TiO_2$, which is controlled by diffusion [38,40]. Beauger et al. [39]. realized a study at the macroscopic interface by superposing the pellets, to explain how barium ions diffuse into the $TiO_2$ boundary. From that, the morphology of the $BaTiO_3$ was found to be determined by the $TiO_2$ particles, which is in agreement with our results. However, the $BaCO_3$ particle sizes define the diffusion rate, which implies to the significant decrease or increase of the temperature in the formation of $BaTiO_3$, as shown in Table 3. In this reaction usually a number of intermediate phases ($Ba_2TiO_4$, $BaTi_4O_9$ and $BaTi_2O_5$), are formed until single phase $BaTiO_3$ is achieved [41,42]. $Ba_2TiO_4$ phase with ICSD number 2625 is detected in BT1-1 and BT2-1 samples (see Fig. 2(b)), whereas, other phases like $BaTi_4O_9$ and $BaTi_2O_5$ are not observed within the detection limit of XRD (1 wt%), as is also shown in Fig. 2(b). Frade and Carter [43,44], built a theoretical model for explaining the reactions between different particles of radius R, which showed that the rate of diffusion is proportional to $1/R^2$. This model is supported by experiments performed for $BaTiO_3$ using $TiO_2$ and $BaCO_3$ as precursors, with particle sizes of nanometer and micrometer, respectively [45,46].

The most critical steps that determine the microstructure and the final properties of powdered ceramics of $BaTiO_3$ are the processing of powders and the thermal treatment. Processing by the solid-state reaction makes use of several solvents (water, acetone, 2-propanol and methanol) to mix the powders of $BaCO_3$ and $TiO_2$ and to thoroughly homogenize the mixture. In this sense, two factors are important to obtain $BaTiO_3$: 1) influence of solvent on the adsorption of organic molecules on the solute particles, after the milling process, and 2) influence of solvent on the particle size of $BaTiO_3$.

The powders are sensitive to the solvent, thus the decomposition of $BaCO_3$ and $TiO_2$ is related to the strength of ionic fields. The Ionic field strength is defined as the charge of an ion divided by the square of its ionic radius [47]. The low ionic field strength of $Ba^{2+}$ (1.11) in comparison to that of $Ti^{4+}$ (8.65), lead to a significant decomposition of $BaCO_3$ in solvent. The degree of decomposition is dependent on the relative basicity scale for the different solvents (pKa), such as: acetone (19.3) > 2-propanol(16.6) > ethanol(15.9) > methanol (15.5) > water (14) [48,49], due to the disproportionation (presence of bound OH) in different solvents as affirmed by Akbas et al. [50]. Such decomposition of $BaCO_3$, easily reacts with $TiO_2$. Likewise, it also suggests that the chemisorption and physisorption onto the surface of the particles could hinder its direct contact with other particles, which reduces the crystalline degree of the $BaTiO_3$ phase due to the presence of the surface chemical defects, after the thermal treatment at low temperature. These effects are explained by the presence of intermediary phases when subjected to the thermal treatment at low temperature [51–58]. Besides the thermal treatment, the contribution to the particle size can be defined on the basis of absence of OH group, i.e. in the acetone, this is because no reaction takes place due to the absence of disproportionation [50]. Contrary, Tomaz et al. [59]. reported that particle sizes of powders increase with increasing water concentration. Table 3 shows that the crystalline phase and particle sizes of the single

**Table 3**
Method of synthesis and particle sizes that have been reported in the literature for $BaTiO_3$ samples.

| Method of synthesis | Particle size $TiO_2$ (nm) | Particle size $BaCO_3$ (nm) | Solvent | Thermal treatment(°C) | Phase formation | Particle size $BaTiO_3$ (nm) | Ref. |
|---|---|---|---|---|---|---|---|
| Solid-state | 67 | 655 | Water | 1000 | C | 253 | [49] |
| Solid-state | 67 | 136 | Water | 900 | C | 135 | [49] |
| Solid-state | 67 | 48 | Water | 800 | I | 112 | [49] |
| Solid-state | 200 | 170/640 | 2-propanol | 900 | I/I | ~200 | [50] |
| Solid-state | 200 | 170 | 2-propanol | 1200 | C | 400 | [50] |
| Solid-state | 100–150 | # | Water | 1000 | C | 150–200 | [54] |
| Solid-state | 16 | 54 | Water | 700/800 | C/C | 70–80 | [55] |
| Solid-state | 28 | 54 | Water | 800 | C | 85 | [55] |
| Solid-state | 700 | 2000 | Methanol | 1150 | I | ~700 | [52] |
| Solid-state | > 1000 | ~1000 | Water | 1100 | I | ~1000 | [51] |
| Solid-state | * | * | Acetone | 1200 | C | > 1000 | [56] |
| Solid-state | 200 | & | Ethanol | 800/1200 | I/C | 240–730 | [53] |
| Solid-state | 30 | & | Ethanol | 800/1200 | C/C | 50–400 | [53] |

I = Incomplete (intermediary phases); C = Complete (single phase); # = urea and $Ba(NO_3)_2$ aqueous solution; & = 50 h of milling.

phase of $BaTiO_3$ are dependent on the: particle sizes of $BaCO_3$ and $TiO_2$, solvent used and on the thermal treatments applied.

### 3.2. IR spectroscopy of adsorbed functional groups on $TiO_2$/$BaCO_3$ particles

The FT-IR absorption spectrum of BT powders, recorded in the wavenumber range of 4000-400 $cm^{-1}$, as a function of different milling times and thermal treatments, are shown in Fig. 8. The set of different bands arising from surface species, the nature of formation of the surface chemical bonds and the products of mixing of different precursors in solvent, were identified. The FT-IR spectrum (Fig. 8(a)) indicated the functional groups on the surface of the precursors to be apparently similar, for different milling times. Likewise, the intensity of the peaks increased with the decrease of the particle size as shown in the SEM images (see Fig. 7).

The IR spectra mainly consisted of four regions. The first region is a broad intense absorption band at 3800-3000 $cm^{-1}$, which arose due to the vibrational stretching of bonded and unbonded hydroxyl groups (OH). Indeed, the broad absorption peak centered at 3442 $cm^{-1}$ corresponds to the OH group of un-dissociated 2-propanol. The intensity and broadness of this band are dependent on the strength of the intermolecular hydrogen bonding in 2-propanol individual molecules. The second region corresponds to the five absorption bands present in the range 3000-2750 $cm^{-1}$. These bands result from the asymmetric and symmetric vibrational stretching of the C–H bonds within the aliphatic alkyl groups (CH, $CH_2$ and $CH_3$), grouped as C–H absorption bands, which corresponds to the decomposition reaction of the 2-propanol. The third region reports an enlarged view of the range 800–1800 $cm^{-1}$, where the characteristic carbonate absorption corresponds to the $\nu(CO_3)$ IR-active vibrational mode and can be evidenced around 900-800 and 1550–1200 $cm^{-1}$. Moreover, a small shoulder at ~1650 $cm^{-1}$ $\delta(H_2O)$, is observed in all milled samples, which is either due to the vibrational stretching of the OH bonds of the water molecules or due to the moisture adsorbed on the external surface of the precursors. The fourth region in the absorption band is the range 800-450 $cm^{-1}$, that corresponds to the bond of $TiO_2$ with OH group. The intensity of absorption in all the spectra increases with increase of the milling time. Such increase is probably related to the reaction process generated from the molecules of 2-propanol, after the absorption of high mechanical energy from the precursors. High mechanical energy and the decrease in the size of the particles subjected to various mixing times, leads to an increase in the available surface area which consequently increases the reaction process due to the availability of more active sites on the surface [21,22]. Based on our FTIR results and the literature [60-63], we assume that the nature of the external surface of precursors is related to the existence of physisorbed and chemisorbed molecules from the decomposition of 2-propanol, after drying. This result also highlights that the high reactivity arises due to the combination of OH with –OR or –R groups (R = $CH_3$, $CH_2CH_3$, $CH(CH_3)_2$) on the external surface of the precursors, when they are exposed to the atmosphere and dried at low temperature, as will be described later.

A mechanism of decomposition reaction between 2-propanol and precursors ($BaCO_3$ and $TiO_2$), can be proposed to explain the chemical transformations and to understand the surface chemistry of the mixture of precursors. The stabilization of the product of the precursors in polar organic solvents, such as 2-propanol and other organic ending groups, is dependent on the solubility, pH value and temperature of the solvent. The solubility of $BaCO_3$ in 2-propanol increases with the decrease in pH value of solvent, owing to the fact that the coefficient of activity of ions varies with ionic strength and pH of the solution [64,65]. Additionally, the formed $TiO_2$ powder agglomerates faster due to its low solubility in organic solvents [11]. Therefore, it can be understood that the mechanism of decomposition reaction occurred simultaneously between the 2-propanol and precursors. The initial value of pH before mixing $BaCO_3$ and $TiO_2$ powders, is only used as a comparison. As a result of mixing, the pH value changed from 7.1 to 4.2, see Table 1. The mechanochemical effects of milling with zirconium oxide balls (0.5 mm) on the mixture were found to be favorable, with low agglomeration, as shown in Fig. 7. Out of a number of possible effects, such as: milling time, decomposition of 2-propanol, degradation and chemical reactions of intermediates, we proposed a reaction mechanism that involves the adsorption of the reactant on a surface-active site, which is summarized in Fig. 9. In this sense, four processes are presented simultaneously: 1) reduction/oxidation mechanism of $TiO_2$ and dissociation of $BaCO_3$, 2) decomposition of 2-propanol, 3) reaction of 2-propanol with itself and with intermediates from the reduction/oxidation mechanism of $TiO_2$, and 4) reaction between $BaCO_3$, dissociated $BaCO_3$ and product generated from processes 1 to 3. Likewise, from the process described, defect generation of $Ti^{3+}$ and $Ba^{2+}$ can be obtained through different processes [66,67], including the grinding jar with grinding balls of 0.5 mm diameter.

For pure 2-propanol, two peaks at 1381 and 1369 $cm^{-1}$ are assigned to the symmetric $\delta_s(CH_3)$ vibrations, while the peaks at 1342 and 1313 $cm^{-1}$ are attributed to the vibrations, δ(CH) and δ(OH), respectively [68,69]. The peak positions at 1164, 1132 and 1113 $cm^{-1}$ are related to the vibrations $\nu$(C–C), $\delta(CH_3)$ and $\nu$(C–O), respectively [70]. The reaction mechanism of both the $BaCO_3$ and $TiO_2$ in 2-propanol solution can be explained by assuming that a molecule of 2-propanol is adsorbed on the external surface of the precursors and is followed by an

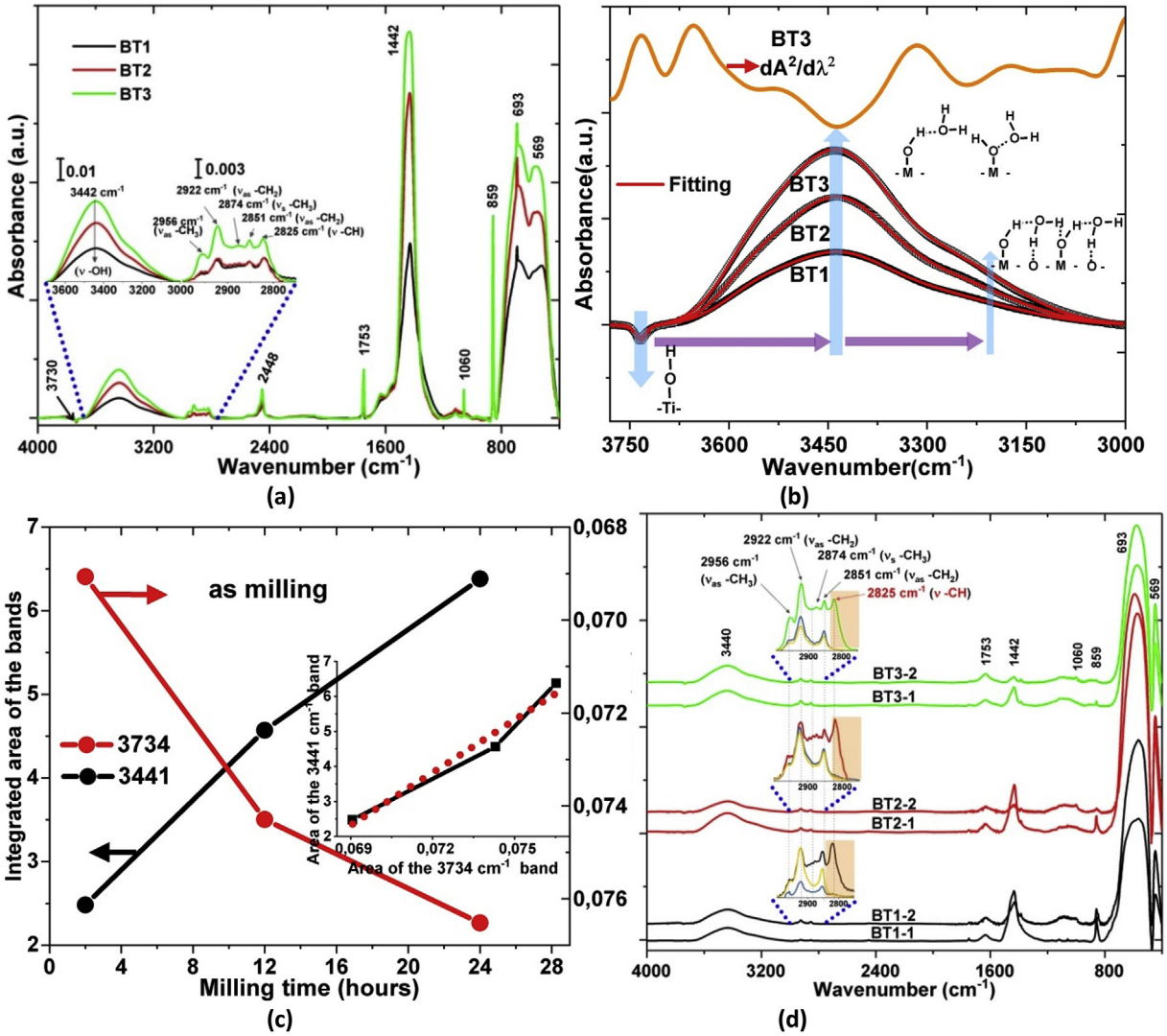


**Fig. 8.** FT-IR analyses for: a) mixed powder at different milling times without thermal treatment, b) a representative kinetic curve as a function of time for hydroxyl group absorption band at 3441 and 3734 $cm^{-1}$, c) hydroxyl group region at different milling times without thermal treatment. The inset in the c) represents the linear relation between absorption at 3441 and 3734 $cm^{-1}$. d) mixed powder at different milling times with thermal treatment.

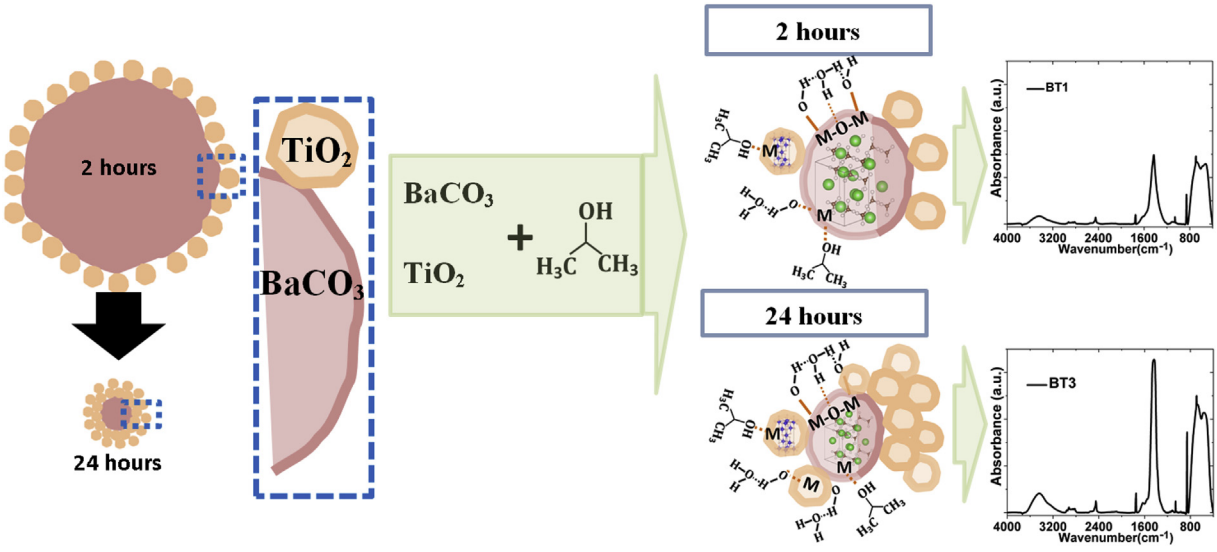


**Fig. 9.** Proposed mechanism for the reaction of 2-propanol over $BaCO_3$ and $TiO_2$, from FT-IR analyses.

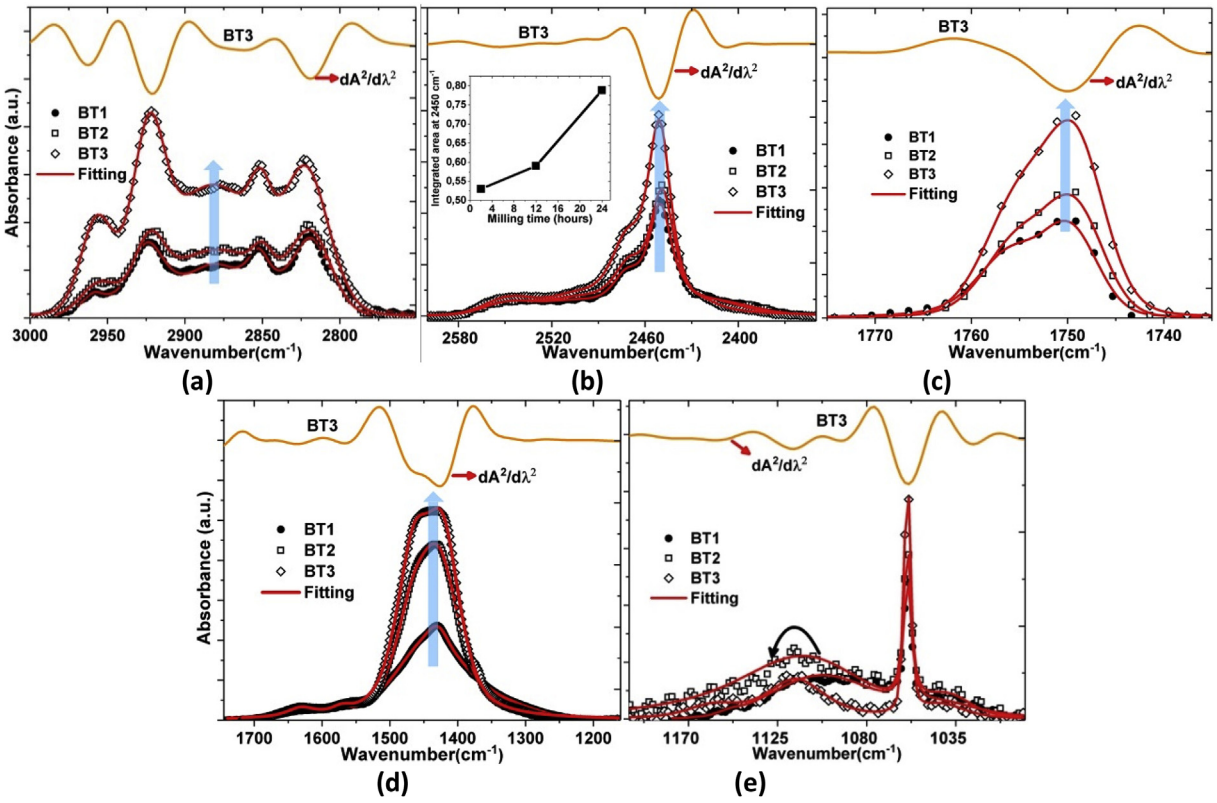


**Fig. 10.** FTIR spectrum and fitting result of BT samples as mixed in different regions a) 2600 to 2360 $cm^{-1}$, b) 1775 to 1735 $cm^{-1}$, c) 1730 to 1170 $cm^{-1}$ and d) 1170 to 1000 $cm^{-1}$.

intramolecular hydrogen bonding and intermolecular electrons transfer by the neighboring hydroxyl groups of the metallic ions (ionic-dipole interaction), represented by M, via oxygen atoms, which resulted in the formation of Ba and Ti ions [71,72], as shown in Fig. 8(b).

Many reports have demonstrated the existence of hydroxyl groups on the anatase $TiO_2$ surface, where Ti–OH bond is the most frequently reported by showing absorption bands pointing upwards (positive bands or positive peak) around 3720 and 3625 $cm^{-1}$. The bands at 3720 and 3625 $cm^{-1}$, are a characteristic of type I and II hydroxyl group, respectively, which is responsible for many degradation processes. The type I is designated to OH group attached to one surface site, while the type II is the OH group bonded to two surface sites, respectively [73]. Fig. 8(a) shows FTIR absorption spectra of $TiO_2/BaCO_3$ mixed after introduction of 2-propanol and subjected to different milling times. The conversion of the absorption positive band of isolated hydroxyl group of $TiO_2$ (Ti–OH) at 3733 $cm^{-1}$ to an absorption negative band (absorption bands pointing downwards) at the same position is observed; see Fig. 8(b). In addition, a loss of OH group from the $TiO_2$ surface is also observed due to the reaction with 2-propanol, and due to the rise of new bands. The overlap of bands between 3650 and 3000 $cm^{-1}$ is associated with different type of hydroxyl groups of acidic-basic character and the $H_2O$ molecules adsorbed through hydrogen bond [74].

Studies reveal strong interaction between the 2-propanol and OH group on $TiO_2$ surface [75–77], which happened in the present case and resulted in chemisorbed alkoxide ions and released $H_2O$ from the condensation of 2-propanol. The release of $H_2O$ was confirmed with the appearance of broad bands at 3442, 3200 and 1630 $cm^{-1}$, see Fig. 8(a). Although the hydroxyl spectra of all samples came similar, the reactivity of the OH groups depend strongly on the particle size, due to existence of more active sites on the surface of precursors. The high intensity band centered at 3442 $cm^{-1}$ is attributed to the physisorbed water molecules, which are bonded by the weak hydrogen bonds with each other and with the OH-groups of $TiO_2$ surface (vacancy-free surface), due to the weak active surface sites. However, the band centered at 3200 $cm^{-1}$ corresponds to the chemisorbed water molecules, strongly bonded onto $TiO_2$ surface. Both, physisorbed and chemisorbed water molecules, are represented in the inset Fig. 8(b). Such bonds are stabilized by the hydrogen bonds with neighboring anions of $TiO_2$ lattice and adjacent bridge of OH-groups, see Fig. 8(b). Additionally, the band centered at 3304 $cm^{-1}$ corresponds to the vibration of the OH group of the physisorbed 2-propanol (undissociated), which is weakly bound with under-coordinated Ti atoms through O atom of the hydroxyl group, inducing the formation of oxygen vacancy. Under-coordinated Ti atoms can also bind through O of hydroxyl via dissociative adsorption of 2-propanol, which results in the chemisorption of alkoxide accompanied by the release of protons ($H^+$) [78].

The band at 3562 $cm^{-1}$ is attributed to barium hydroxide hydrate [79], where the water molecules form strong hydrogen bridges with $Ba^{+2}$ ions (dissociation of $BaCO_3$) [80]. All the peaks were identified from the deconvolution of spectra. The most important fact is the linear increase of the area of both the negative band at 3733 $cm^{-1}$ (O–H stretching of Ti–OH) and the positive band at 3442 $cm^{-1}$ (O–H stretching of $H_2O$), respectively, as shown in Fig. 8(c). This trend became clearer when the milling time increased, see inset Fig. 8(c). These correlations indicate the change of state of hydrogen atoms from isolated to bonded, with the physisorbed water molecules, which induce shifting of the OH band by -340 $cm^{-1}$. The release of water, from the condensation of 2-propanol, physisorbed on the metallic surface, can also be evidenced by the band at 1632 and 1115 $cm^{-1}$ (OH), suggesting that $H_2O$ was formed during the adsorption process or produced by the thermal dehydration of 2-propanol [63]. Therefore, a decrease in the particle size due to milling time, is associated to the rise of oxygen vacancies (structural defect) and to the defect chemistry, simultaneously. This improves both the formation of the OH groups on the $TiO_2$ surface and promotes the reaction process 1 (Fig. 9). It also

promotes the formation of intermediates with 2-propanol through the decomposition reaction. Other contributions also give rise to the formation of water molecules from: a) reduction/oxidation mechanism, b) interaction between 2-propanol and the product generated from the reduction/oxidation mechanism, c) decomposition of 2-propanol and d) 2-propanol reaction with itself. It is interesting to note that the higher the chemisorbed water amount is, the higher the physisorbed water quantity becomes. This is because weak hydrogen bond with each other and with OH-groups of $TiO_2$ surface acts as an adsorption site for the water molecules, released from the reaction of Ti–OH with 2-propanol and ambient water.

The band at ~3304 $cm^{-1}$ (OH hydroxyl group), is assigned to the physisorbed and undissociated 2-propanol, that is weakly bound via O atoms of the hydroxyl, with under-coordinated Ti atoms (confirmed as Ti–$OHCH(CH_3)_2$), which further leads to the appearance of new absorption bands at 2956, 2922, 2874, 2851, 2825, 1569, 1464, 1385, 1298, 1170 and 1135 $cm^{-1}$, see Fig. 10(a,d and e). On the other hand, the reaction of OH group on $TiO_2$ surface and 2-propanol, gives rise to water molecules (3442, 3200 and 1632 $cm^{-1}$) and chemisorbed alkoxy groups. Other more stable product generated is the propene [77,81,82]. In both cases, the reduction/oxidation mechanism alone has no effect on the reactivity of the absorbed 2-propanol, however, in atmospheric pressure it exhibits higher reactivity, leading to the formation of intermediates, as shown in the process 1. The atmosphere $O_2$ can trap electrons and result in the formation of superoxide radical ions $O_2^{\bullet-}$, where, oxygen atoms can react with hydroxyl groups and can bind to the $TiO_2$ surface (Ti–OH), forming water molecules [83]. In addition, oxygen atoms can be trapped by oxygen vacancies onto the $TiO_2$ surface.

Due to the lower stability of alkoxide group, as an intermediate product, the stabilization of corresponding reactions mainly reaches through the formation of acetone and methoxy group. Due to the lower stability of alkoxyde groups, these may undergo a successive dehydrogenation through deprotonation (removal of a hydrogen atom), resulting in the breakage of C–H bond and thus becoming oxidized, giving rise to Ti–O═$C(CH_3)_2$, which consequently corresponds to the weakening of ionic Ti–O bond. This absorption band of Ti–O═$C(CH_3)_2$ is confirmed by the IR analysis and evidenced by the presence of C═O band at 1748 $cm^{-1}$, which is a characteristic of the carbonyl group in ketones, see Fig. 10(c). Thereafter, the process of conversion of the ketone on dehydrated $TiO_2$ (or metal ions), due to the mechanical energy or by drying at low temperature, leads to the formation of products that can be confirmed by the absorption bands at 2956, 2874, 2452, 1566, 1427 and 1384 $cm^{-1}$, as shown in Fig. 10(a,d). These bands formed are attributed to the several functional groups on the $TiO_2$ surface, including absorbed $CO_2$ and monodentate formate. However, other peaks could also appear due to the release of molecules during the oxidation process of acetone, such as monodentate formate on $Ba^{2+}$ cations [84]. Therefore, the formation of main intermediate products such as: methoxy [78], propene [77,81,82], alkoxy [85,86], acetaldehyde [78,86] and propanone [87] group and the result of their dissociation reaction in the form of $CO_2$, $H_2O$ and $OH^-$, among others, plays an important role in bonding with $BaCO_3$ molecules and in their dissociation, as suggested by the model based on the $CO_3^{2-}$ anions and $Ba^{+2}$ cations.

The intense peak at 2452 $cm^{-1}$ is assigned to the adsorbed $CO_2$ due to the oxidation of acetone. The $O^-$ can react with adsorbed acetone, resulting in $CO_2$ that gets adsorbed on the superface of the particles. It is shown that the increase in the intensity of the adsorbed gas-phase $CO_2$ product on the surface of the particles, is an indication of high activity of the metallic system for this reaction, which is dependent on the conditions of milling time and thermal treatment. The $CO_2$ molecule has three important vibrational modes; the symmetric stretching $\nu_1$(1388 $cm^{-1}$) that is only Raman active, the double degenerate $\nu_2$(667 $cm^{-1}$) bending mode, and the asymmetric stretching $\nu_3$(2349 $cm^{-1}$) [88]. Bollinger and Vannice [62] observed a similar feature at around 1669 $cm^{-1}$ assigned to the bicarbonate species, when $CO_2$ was introduced on to 1 wt% Au/$TiO_2$ catalyst. Boccuzzi et al. [89] have also attributed the band at 1670 $cm^{-1}$ to carbonate like species on Au/$TiO_2$ catalyst. Acetates can also be oxidized and produce carbonates directly on the surface of the particles. However, the intense peak at 2452 $cm^{-1}$ is shifted with respect to the peak at 2349 $cm^{-1}$ for free $CO_2$, which can also be due to the $CO_2$ absorption onto the $Ba(OH)_2$ metallic hydroxides (peak at 3733 $cm^{-1}$).

Several shoulders around 2452 $cm^{-1}$ at 2554, 2533, 2473 and 2421 $cm^{-1}$ are observed with a shift, shown in Fig. 10(b). This shift can be explained in terms of a progressive solvation of metallic hydroxides by $CO_2$ molecules, with the formation of $Ba(OH)_2(CO_2)$, as already pointed out by Pragati et al. and Llabrés et al. [88,90]. Both of them reported the shift to high frequencies with respect to the free $CO_2$ molecules, that owed to the $CO_2$ interaction with different ions ($Na^+$ and $Mg^{2+}$). Garrone et al. [91] also used computational study (DFT) of absorption of $CO_2$ on $Li^+$, $Na^+$, and $K^+$ ions, determining the vibrational frequency of each cation, which lied in a wide window between 2460 and 2426 $cm^{-1}$. Additionally, the formation of $Ba(OH)_2$, described before, can be obtained from different processes as shown in Fig. 9. The pH in 2-propanol was 6.8, which varied according to the milling time pH = 7.1 (2 h) to pH = 4.2 (24 h). These values are considered allowed for the reaction described in Fig. 9, where the reaction, $Ba^{2+} + OH^-$, can be ignored if the solution is acidic [64]. Li et al. [64]. assumed that the formation of $Ba(OH)_2$, $BaOH^+$, $BaHCO_3$ and $Ba(HCO_3)_2$ is much smaller than the formation of $Ba^{2+}$ in basic solution. Three factors can be assumed that could increase the formation of $Ba(OH)_2$, $BaOH^+$, $BaHCO_3$ and $Ba(HCO_3)_2$ in the organic solvents; 1) the presence of $TiO_2$, via water condensation from the reaction between two hydroxylates, 2) the milling time, that allows to create more active sites on the surface, and 3) the product which comes as a result of mixing of the organic solvent with the precursors yield a sub-product and gives rise to hydroxyl groups among others. Fig. 10(b) shows the increase of $CO_2$ absorbed on the $Ba(OH)_2$ metallic hydroxides as a function of milling time, where a linear correlation is verified, see inset of Fig. 10(b).

The complexity of this mechanism, and of the resulting product mixtures, suggest that many of the various intermediates formed during the course of reaction, takes part in further reactions with carbon dioxide, bicarbonate and carbonic acid. The release of water, from the hydrolysis and condensation of alkoxide group can also be evidenced by the bands at 1632 and 1115 $cm^{-1}$ (OH) [63]. Referring to the literature, $H_2O$ may also be produced by the thermal dehydration of 2-propanol [92]. In this work, it is observed that, drying of the solvent of the mixture of precursors at low temperature (~60 °C) does not favor such process, as C═C band at 1660 $cm^{-1}$ is not observed. Both bands (1632 and 1115 $cm^{-1}$), are attributed to the di-hydrated barium carbonate $BaCO_3{\cdot}2(H_2O)$. The transformation of $BaCO_3{\cdot}2(H_2O)$ from $BaCO_3$ can be identified from the frequency variation between both bands ($\Delta\nu$ = 517 $cm^{-1}$), which can be interpreted as the distortion (less coordinated state) from the symmetric $CO_3^{2-}$ anions of carbonate which confirms the formation of hydrated barium carbonate. These observations are consistent with what has been previously observed [63,93]. A broad shoulder, centered around 1566 $cm^{-1}$ is a characteristic of the $\nu_{as}$(-$COO^-$) vibration mode of monodentate formate species adsorbed on the $TiO_2$ surface, as mentioned before.

The two bands at 1465 and 1384 $cm^{-1}$ are assigned to the asymmetric and symmetric stretching vibrations of $CH_3$, see Fig. 10(d). Both methyl C–H bands correspond to the non-dissociative absorption mode of 2-propanol. However, Baltrusaitis et al. [94], attributed both peaks at 1465 and 1384 $cm^{-1}$ to the monodentate absorbed carbonate, i.e. $CO_3^{2-}$ interacting with $Ba^{2+}$ cations. These peaks are deconvoluted using the mixed of the Gaussian and Lorentzian function to fit curve, see Fig. 10 (d). The similarity in the peak positions is likely due to the methyl termination group (C–H), present in both peaks. Four main absorption bands which are characteristic of the vibration in carbonate

anion ($CO_3^{2-}$) isolated by $Ba^{2+}$, from $BaCO_3$, are observed and can be identified by the bands at 1427, 1059, 857 and 693 $cm^{-1}$, as shown in Fig. 10(d,e). Such bands are associated to the asymmetric and symmetric stretching vibrations of C–O, out of plane bending vibrations of $CO_3^{2-}$ and in plane bending vibrations of $CO_3^{2-}$, respectively. Finally, absorption bands at wavenumbers less than 800 $cm^{-1}$ which are related to the M-O bands are observed, which result from the Ti–O and Ti–O–Ti bands [95].

It should be mentioned that the intensity maximum and position of the bands depends on the milling time, especially in case of the samples with milling time of 24 h (BT3), where a slight shift to lower wavenumber (1420 $cm^{-1}$) is observed with increase in milling times, see Fig. 10. The increase in the intensity is related to the decrease of the particle size which leads to an increase in available surface area and consequently increases the reaction process due to the availability of more number of active sites on the surface.

### 3.3. Temperature dependent infrared spectra of adsorbed functional groups on $BaTiO_3$ particles

Under thermal conditions at high temperature 1000 and 1100 °C, the organic compound results in a depletion on the surface of precursors, shown in Fig. 11. Such depletion might vary according to the milling time and temperature. However, this depletion, after the thermal treatment, appeared highly dependent on the structure of the organic compound in the spectra and is followed by a nucleation, crystallization and growth process in the heating stage. The crystallization process involved diffusion of $Ba^{2+}$ into the undissolved $TiO_2$, that resulted in the formation of the $BaTiO_3$ phase. However, the reaction of different groups and radicals generated through all the four processes could be responsible for the formation of secondary phases after thermal treatment, as shown in the XRD Fig. 2(b) (sample BT1-1 and BT2-1). Fig. 8 (d) shows the FT-IR spectra taken for thermally treated powders treated at temperatures 1000 and 1100 °C. In the BT1-1 and BT1-2 samples, the broad intense absorption band at 3700-3000 $cm^{-1}$ associated to the OH bands, is found to remain practically unchanged with the temperature variation. This indicates that the removal of physisorbed and chemisorbed water molecules and chemisorbed alkoxide ions on the metallic surface after heating at 1000 and 1100 °C is negligible, see Fig. 11(a). In contrast, the BT1-1/BT2-2 and BT3-1/BT3-2 samples, indicated greater decomposition of physisorbed water molecules than chemisorbed water molecules. The absorption in the range 3000-2750 $cm^{-1}$ in all samples after thermal treatment, present four bands, in comparison to the samples not treated thermally, where the fifth peak at 2825 $cm^{-1}$ within the absorption bands of C–H is not present, see Fig. 11 (a). The absorption bands are attributed to the alkoxide, methoxy ($CH_3O$) and ethoxy ($CH_3CH_2O$) groups, resulting from the decomposition of intermediate products in to methanol ($CH_3OH$) and ethanol ($CH_3CH_2OH$), as described previously, and are associated with the absorption band at 1000 - 1250 $cm^{-1}$. After thermal treatment at 1000 and 1100 °C, the absorption features due to $CH_3OH$, $CH_3CH_2OH$, $CH_3O$ and $CH_3CH_2O$ almost disappeared, as indicated by the reduction in the relative intensity of the peaks at 2956, 2922, 2874 and 2852 $cm^{-1}$. This reduction becomes significant in samples with milling time of 2 h. Such decrease is associated to the breakage of C–H bonds at high temperature. A complete decomposition of alkoxide group can be evidenced, by Fig. 11(a) (dashed lines). The presence of the four peaks at 2956, 2922, 2874 and 2852 $cm^{-1}$, confirms complexity of BT with $CH_3O$ and $CH_3CH_2O$ group. The relative intensity of the peaks in the range 3000 to 2750 $cm^{-1}$, for each sample is determined from the integrated area taken from the deconvoluted spectra, Fig. 11(d).

A significant decrease of C=O band at 1748 $cm^{-1}$ is observed, principally in the samples with milling time of 12 and 24 h and

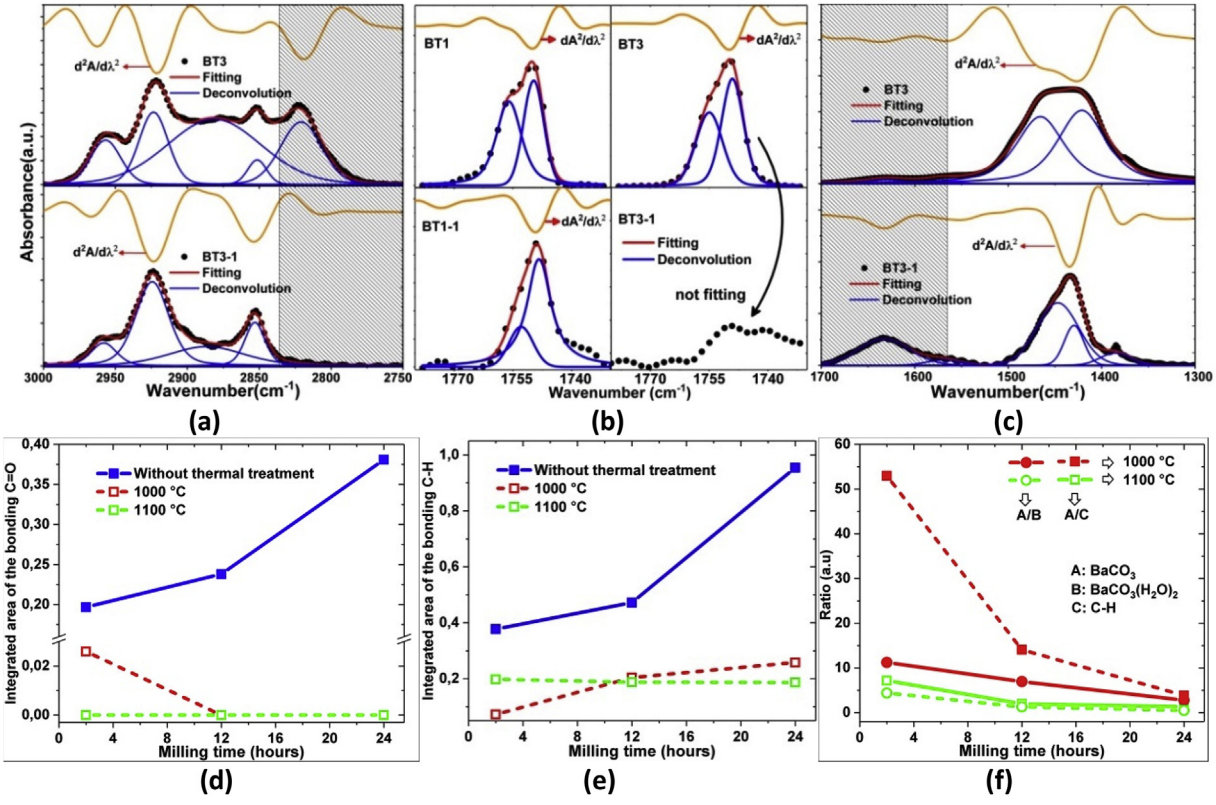


**Fig. 11.** Fragments of FTIR spectra and deconvolution spectral bands (solid blue line) in the different regions, a) 3000 to 2750 $cm^{-1}$, b) 1775 to 1735 $cm^{-1}$, c) 1730 to 1300 $cm^{-1}$ and d) 1170 to 980 $cm^{-1}$. Solid red line presents the sum of the blue solid line shapes. (e) Variation of C–H group intensity as a function of milling time (f) ratio of $BaCO_3$/C=O and $BaCO_3$/C–H as a function of milling time. (For interpretation of the references to colour in this figure legend, the reader is referred to the Web version of this article.)

thermally treated at 1000 and 1100 °C, as shown in Fig. 11(b). This decrease is linked to the breaking of carbonyl group in acetone, Ti–O═C($CH_3$)$_2$, which allowed the formation of tetragonal structure of $BaTiO_3$. Fig. 11(d), shows the evolution of the absorption band at 1748 $cm^{-1}$ as a function of milling time, which can be assigned to $\nu$(C═O) of the acetone. The tendency of the increase in the absorption of acetone depends of the amount of the surface sites on the $TiO_2$ surface, which increases with the increase in milling time. The breaking of C═O binding is observed significant in all thermally treated samples, except the sample BT1-1, which showed a small absorption, see Fig. 11(b,d).

The peak positions due to the absorption of $CH_3O$ and $CH_3CH_2O$ group appeared quite similar, this indicated that the absorption bands in the range 1000–1250 $cm^{-1}$ could represent a peak overlap, that arises due to the stretching vibrations of C–O and C–C of the $CH_3O$ and $CH_3CH_2O$ absorption groups on the $TiO_2$ surface, as shown in Table 3. The absorption band at 1041 and 1116 $cm^{-1}$ reflects the presence of bidentate and monodentate formate species (C–O stretching vibration) of $CH_3O$ group on the $TiO_2$, respectively, while the peak at 1058 $cm^{-1}$ is assigned to the C–C stretching vibration from $CH_3CH_2O$ [85,86]. After thermal treatment, the intensity of the absorption band of $CH_3O$ and $CH_3CH_2O$ group, significantly reduced due to its decomposition and removal from the surface. Alongside, a decrease in the intensity of bands at 2956, 2922, 2874, 2851, 2825, 1590, 1489, 1464, 1385, 1170 and 1135 $cm^{-1}$, is observed after thermal treatment, as shown in Fig. 11(a,c).

Thermal treatment indicates that part of the physisorbed $H_2O$ and 2-propanol can be removed. This result shows that bidentate and monodentate formate species of $CH_3O$ and $CH_3CH_2O$ groups possess similar thermal stability at high temperature. In addition, thermal treatment can also promote the creation of more Lewis acid or base sites on the surface, as suggested by Trikalitis et al. [81]. In this sense, in the perovskite (***AB***$O_3$) structure, the A-site contain an alkaline element, while the B-site accommodate a transition metal. The ***A***-site (Ba), does not have the ability to decompose to the 2-propanol, since it has single state of oxidation. However, the ***B***-site (Ti) due to the possibility of different oxidation states of Ti ($Ti^{2+}$, $TiO^{3+}$, and $TiO^{4+}$), is able to suffer oxidation-reduction process even in the presence of 2-propanol. It is because different oxidation states accounts for the different number of electrons in the 3d orbital which helps in the oxidation-reduction process. In order to evaluate the acidic and basic character of *A* and *B* sites, the Smith's acid-base parameter "δ" was evaluated [96] and modified from the relations between "δ" and electronegativity χ [97], respectively. Where "δ" is a constant which measure the tendency to accept an oxide ion. Smith assigned the parameter $\delta < 0$ to basic or amphoteric, while $\delta > 0$ to acidic nature. For $TiO_2$ the value $\delta_{TiO_2} = 0.7$ is observed, while for $BaCO_3$ the value of $\delta_{BaCO_3} = -4.6$ is observed which was determined from the relations between "δ" and electronegativity χ. Similar arguments by Kuhn et al. [98], correlated the Lewis acid sites to A cations, while basic sites were associated with B cations, which is a result contrary to Natile et al. [99], who correlated Lewis acid sites to B cations. Likewise, as shown in Fig. 11 (e) the variation of the absorption bands in the range 3000 to 2700 $cm^{-1}$ indicates that the reduction occurred rapidly with thermal treatment at 1000 and 1100 °C. Fig. 11(f) shows the ratio of integrated area of the carbonate absorbed to the di-hydrate carbonate and carbonate absorbed to C–H bond, as a function of milling time and thermal treatment. For the samples with milling time of 2 h and thermal treatment of 1000 °C, the ratio A/B evidenced an enrichment of secondary phase, which is according to the XRD results, that demonstrated the presence of $BaCO_3$ as a secondary phase, contrarily at high temperature (1100 °C) the ratio A/B is observed to be smaller. Besides, the ratio A/C decreased progressively with increased in milling time and temperature, this ratio is five times greater than the ratio A/B for the samples thermally treated at 1000 °C. The presence of secondary phase indicated the absence of complete reaction between $BaCO_3$ and $TiO_2$, which could be due to the C═O group strongly bonded to $TiO_2$ at low temperature, see Fig. 11(d). The pure phase was observed in all samples, except the BT1-1 and BT2-1 (presence of $BaCO_3$, $TiO_2$ and $Ba_2TiO_4$), with the help of FTIR spectroscopy within the detection limit of XRD (1 wt%). Therefore, the thermal treatment contributes to the release of defects, principally the hydroxyl ions ($OH^-$), protons ($H^+$) and carbonates ($CO_3^{2-}$), which gets bonded to the surface of the structure of $BaCO_3$ and $TiO_2$ during the milling process.

In this work, we proposed that the bonds of different intermediates, arise from the decomposition of 2-propanol, over the surface of $BaTiO_3$, as explained before. The alcohol group of 2-propanol and of the products of intermediate reactions (which are initially bound to the surface of $TiO_2$, $BaCO_3$ and to the dissociation of $BaCO_3$), remain bounded to the Lewis acidic or basic sites, through the bridged oxygen atoms, after thermal treatment. We associate the bonds on the surface of $BaTiO_3$ structure (which involves adsorption of the reactant over an active site), to be mainly responsible for the dissociation of 2-propanol to form intermediates. Fig. 9 shows the formation of different bonds after the thermal treatment, which were also experimentally confirmed by the FTIR spectra.

It is important to note that the points mentioned above are prompted to find alternative explanations for the reaction mechanism between the precursors and the solvent, and consequently to explain the formation process of $BaTiO_3$. The hydroxyl groups associated with water molecules are present in high concentrations due to the milling, which breaks the particles (accompanied for hydrolysis and condensation) and plays a great role in the dissociation of carbonate. In addition, the presence of water molecules decreases the interaction between the carbonate species and monodentate carbonate with the surface, which can induce the distortion of the geometry of $BaTiO_3$ (reflected in the shift of peaks and variation of intensity), after thermal treatment. Therefore, both un-dissociated and dissociated 2-propanol along with intermediates are present in the samples as a mixture on the surface. These dissociated propanol and intermediates are present even after the thermal treatments. Hence, these factors must be considered in order to describe the properties associated to the structure of $BaTiO_3$.

## 4. Conclusion

In this work, we provided a detailed investigation and understating on the surface properties and reactivity of the mixing of the $BaCO_3$ and $TiO_2$ precursors in organic 2-propanol solvent, in different milling times and thermal treatments. The absorption behavior was studied by the FTIR spectroscopy. The characterization by XRD revealed: 1) a gradual decrease in the tetragonality (c/a) of $BaTiO_3$ with the decrease of particle size at thermal treatment of 1000 °C. Contrarily, an enhancement in the tetragonality was found with the decrease of particle size and after the application of high temperature (1100 °C). The strain observed for the structure by the milling process from 2 to 24 h increased, which was significantly higher for samples thermally treated at 1100 °C than at 1000 °C. The results of FTIR indicated that both chemisorbed and physisorbed 2-propanol are present on the surface of $TiO_2$ and $BaCO_3$, where it was found significantly present in the later. The process started from the strong interaction between the 2-propanol and OH groups on the $TiO_2$ surface which gave rise to chemisorbed alkoxide ions and released $H_2O$. The product generated from the reaction process gave rise to the inorganic-organic matter association. However, the functional group associated to the $BaCO_3$ and $TiO_2$ resulted in a depletion on the surface at high temperature. This work did not only manifest the importance of understating of the structural level, but also helped to evaluate the surface structure of the $BaTiO_3$ samples.

## Acknowledgments

This research was supported by Instituto de Física de São Carlos - Universidade de São Paulo (IFSC-USP) and Conselho Nacional de

Desenvolvimento Científico e Tecnológico (CNPq) (project number 158934/2018-0) through the Centro de Pesquisa em Óptica e Fotônica (CePOF), São Paulo, Brazil, with project 2013/07276-1.

## Appendix A. Supplementary data

Supplementary data to this article can be found online at https://doi.org/10.1016/j.ceramint.2019.09.296.

## References


[1] Y. Tan, J. Zhang, Y. Wu, C. Wang, V. Koval, B. Shi, et al., Unfolding grain size effects in barium titanate ferroelectric ceramics, Sci. Rep. 5 (2015) 15–21, https://doi.org/10.1038/srep09953.

[2] J. Suntivich, K.J. May, H.A. Gasteiger, J.B. Goodenough, Y. Shao-Horn, A perovskite oxide optimized for oxygen evolution catalysis from molecular orbital principles, Science 334 (2011) 1383–1385, https://doi.org/10.1126/science.1212858 80.

[3] S. Liu, L. Huang, W. Li, X. Liu, S. Jing, J. Li, et al., Green and scalable production of colloidal perovskite nanocrystals and transparent sols by a controlled self-collection process, Nanoscale 7 (2015) 11766–11776, https://doi.org/10.1039/c5nr02351c.

[4] D. Erdem, N.S. Bingham, F.J. Heiligtag, N. Pilet, P. Warnicke, C.A.F. Vaz, et al., Nanoparticle-based magnetoelectric BaTiO3-CoFe2O4 thin film heterostructures for voltage control of magnetism, ACS Nano 10 (2016) 9840–9851, https://doi.org/10.1021/acsnano.6b05469.

[5] J.L. Clabel H, F.L. Zabotto, I.C. Nogueira, P. Schio, D. Garcia, O.F. De Lima, et al., Magnetoelectric properties of laminated La0.7Ba0.3MnO3-BaTiO3 ceramic composites, J. Magn. Magn. Mater. 364 (2014) 18–23, https://doi.org/10.1016/j.jmmm.2014.04.014.

[6] J.L. Clabel H, F.A. Ferri, F.L. Zabotto, V.A.G. Rivera, I.C. Nogueira, D. Garcia, et al., Grain size and interfacial interdiffusion influence on the magnetic and dielectric properties of magnetoelectric La0.7Ba0.3MnO3–BaTiO3 composites, J. Magn. Magn. Mater. 407 (2016) 160–166, https://doi.org/10.1016/j.jmmm.2016.01.082.

[7] M.K. Mahata, K. Kumar, V.K. Rai, Structural and optical properties of Er3 + / Yb3 + doped barium titanate phosphor prepared by co-precipitation method, Spectrochim, Acta Part A Mol. Biomol. Spectrosc. 124 (2014) 285–291, https://doi.org/10.1016/j.saa.2014.01.014.

[8] W.S. Yun, J.J. Urban, Q. Gu, H. Park, Ferroelectric properties of individual barium titanate nanowires investigated by scanned probe microscopy, Nano Lett. 2 (2002) 447–450, https://doi.org/10.1021/nl015702g.

[9] L. Wu, M.C. Chure, K.K. Wu, W.C. Chang, M.J. Yang, W.K. Liu, et al., Dielectric properties of barium titanate ceramics with different materials powder size, Ceram. Int. 35 (2009) 957–960, https://doi.org/10.1016/j.ceramint.2008.04.030.

[10] G. Li, N.M. Dimitrijevic, L. Chen, J.M. Nichols, T. Rajh, K. a Gray, The important role of tetrahedral $Ti^{4+}$ sites in the phase transformation and photocatalytic activity of $TiO_2$ nanocomposites, J. Am. Chem. Soc. 130 (2008) 5402–5403, https://doi.org/10.1021/ja711118u.

[11] H. Kominami, J.I. Kato, S.Y. Murakami, Y. Kera, M. Inoue, T. Inui, et al., Synthesis of titanium(IV) oxide of ultra-high photocatalytic activity: high-temperature hydrolysis of titanium alkoxides with water liberated homogeneously from solvent alcohols, J. Mol. Catal. A Chem. 144 (1999) 165–171, https://doi.org/10.1016/S1381-1169(98)00350-1.

[12] R.E. Carter, Kinetic model for solid-state reactions, J. Chem. Phys. 34 (1961) 2010–2015, https://doi.org/10.1063/1.1731812.

[13] M. Bradley, Curve fitting in Raman and IR Spectroscopy : basic theory of line shapes and applications, thermo fish, Science 80 (2007) 0–3 http://thermo.fr/eThermo/CMA/PDFs/Product/productPDF_57565.PDF.

[14] J.P.R. De Villiers, Crystal structures of aragonite, strontianite, and witherite, Am. Mineral. 56 (1971) 758–767 http://www.minsocam.org/ammin/AM56/AM56_758.pdf.

[15] M. Horn, C.F. Schwerdtfeger, E.P. Meagher, Refinement of the structure of anatase at several temperatures, Z. Kristal. New Cryst. Struct. 136 (1972) 273–281, https://doi.org/10.1524/zkri.1972.136.3-4.273.

[16] R. Ashiri, On the solid-state formation of BaTiO3 nanocrystals from mechanically activated BaCO3 and TiO2 powders: innovative mechanochemical processing, the mechanism involved, and phase and nanostructure evolutions, RSC Adv. 6 (2016) 17138–17150, https://doi.org/10.1039/C5RA22942A.

[17] R.H. Buttner, E.N. Maslen, Structural parameters and electron difference density in BaTiO3, Acta Crystallogr. Sect. B Struct. Sci. 48 (1992) 764–769, https://doi.org/10.1107/S010876819200510X.

[18] K. Momma, F. Izumi, VESTA 3 for three-dimensional visualization of crystal, volumetric and morphology data, J. Appl. Crystallogr. 44 (2011) 1272–1276, https://doi.org/10.1107/S0021889811038970.

[19] S.W. Kwon, D.H. Yoon, Dependence of the cyrstal structure on particle size in barium titanate, J. Am. Ceram. Soc. 72 (1989) 1555–1558.

[20] M. Frey, D. Payne, Grain-size effect on structure and phase transformations for barium titanate, Phys. Rev. B. 54 (1996) 3158–3168, https://doi.org/10.1103/PhysRevB.54.3158.

[21] D.H. Yoon, Tetragonality of barium titanate powder for a ceramic capacitor application, J. Ceram. Process. Res. 7 (2006) 343–354.

[22] S.W. Kwon, D.H. Yoon, Tetragonality of nano-sized barium titanate powder prepared with growth inhibitors upon heat treatment, J. Eur. Ceram. Soc. 27 (2007) 247–252, https://doi.org/10.1016/j.jeurceramsoc.2006.02.031.

[23] Y. Sakabe, N. Wada, Y. Hamaji, Grain size effects on dielectric properties and crystal structure of fine-grained BaTiO 3 ceramics, J. Korean Phys. Soc. 32 (1998) 260–264.

[24] L.V. Leonel, A. Righi, W.N. Mussel, J.B. Silva, N.D.S. Mohallem, Structural characterization of barium titanate-cobalt ferrite composite powders, Ceram. Int. 37 (2011) 1259–1264, https://doi.org/10.1016/j.ceramint.2011.01.017.

[25] S.W. Kwon, D.H. Yoon, Effects of heat treatment and particle size on the tetragonality of nano-sized barium titanate powder, Ceram. Int. 33 (2007) 1357–1362, https://doi.org/10.1016/j.ceramint.2006.05.008.

[26] H. Ahamed, V. Senthilkumar, Role of nano-size reinforcement and milling on the synthesis of nano-crystalline aluminium alloy composites by mechanical alloying, J. Alloy. Comp. 505 (2010) 772–782, https://doi.org/10.1016/j.jallcom.2010.06.139.

[27] X.H. Zhu, J.M. Zhu, S.H. Zhou, Z.G. Liu, N.B. Ming, D. Hesse, BaTiO3 nanocrystals: hydrothermal synthesis and structural characterization, J. Cryst. Growth 284 (2005) 486–494, https://doi.org/10.1016/j.jcrysgro.2005.05.080.

[28] V.P. Pavlović, D. Popović, J. Krstić, J. Dojčilović, B. Babić, V.B. Pavlović, Influence of mechanical activation on the structure of ultrafine BaTiO3 powders, J. Alloy. Comp. 486 (2009) 633–639, https://doi.org/10.1016/j.jallcom.2009.07.008.

[29] M.M. El-Khabeery, M. Fattouh, Residual stress distribution caused by milling, Int. J. Mach. Tool Manuf. 29 (1989) 391–401, https://doi.org/10.1016/0890-6955(89)90008-4.

[30] Y. Shiratori, C. Pithan, J. Dornseiffer, R. Waser, Raman scattering studies on nanocrystalline BaTiO 3 Part I – isolated particles and aggregates, J. Raman Spectrosc. 38 (2007) 1288–1299, https://doi.org/10.1002/jrs.

[31] C. Gomez-Yanä, C. Benitez, H. Balmori-Ramirez, Mechanical activation of the synthesis reaction of BaTiO 3 from a mixture of BaCO 3 and TiO 2 powders, Ceram. Int. 26 (2000) 271–277, https://doi.org/10.1016/S0272-8842(99)00053-X.

[32] B.D. Stojanovic, A.Z. Simoes, C.O. Paiva-Santos, C. Jovalekic, V.V. Mitic, J.A. Varela, Mechanochemical synthesis of barium titanate, J. Eur. Ceram. Soc. 25 (2005) 1985–1989, https://doi.org/10.1016/j.jeurceramsoc.2005.03.003.

[33] C.H. Kim, K.J. Park, Y.J. Yoon, D.S. Sinn, Y.T. Kim, K.H. Hur, Effects of milling condition on the formation of core-shell structure in BaTiO3grains, J. Eur. Ceram. Soc. 28 (2008) 2589–2596, https://doi.org/10.1016/j.jeurceramsoc.2008.03.030.

[34] M.F.S. Alves, R.A.M. Gotardo, L.F. Cótica, I.A. Santos, W.J. Nascimento, D. Garcia, et al., High density nanostructured BaTiO3ceramics obtained under extreme conditions, Scr. Mater. 66 (2012) 1053–1056, https://doi.org/10.1016/j.scriptamat.2012.02.044.

[35] A.E.R. Westman, The packing of particles, J. Am. Ceram. Soc. 13 (1930) 767–779, https://doi.org/10.1111/j.1151-2916.1936.tb19809.x.

[36] A.E.R. Westman, The packing of particles: empirical equations f o r intermediate diameter ratios, J. Am. Ceram. Soc. 19 (1935) 127–129.

[37] T. Ng, W. Zhou, G. Ma, X. Chang, International Journal of Solids and Structures Macroscopic and microscopic behaviors of binary mixtures of different particle shapes and particle sizes, Int. J. Solids Struct. 135 (2018) 74–84, https://doi.org/10.1016/j.ijsolstr.2017.11.011.

[38] A. Beauger, J.C. Mutin, J.C. Niepce, Synthesis reaction of metatitanate BaTiO3 - Part 1 Effect of the gaseous atmosphere upon the thermal evolution of the system BaCO3-TiO2, J. Mater. Sci. 18 (1983) 3041–3046, https://doi.org/10.1007/BF00700786.

[39] A. Beauger, J.C. Mutin, J.C. Niepce, Synthesis reaction of metatitanate BaTiO3 - Part 2 Study of solid-solid reaction interfaces, J. Mater. Sci. 18 (1983) 3543–3550, https://doi.org/10.1007/BF00540726.

[40] L.K. TEMPLETON, J.A. PASK, formation of BaTiO3 from BaCO3 and TiO2 in air and in CO2, J. Am. Ceram. Soc. 42 (1959) 212–216, https://doi.org/10.1111/j.1151-2916.1959.tb15455.x.

[41] T.T. Lee, C.Y. Huang, C.Y. Chang, S.P. Lin, C.Y. Su, C. Te Lee, et al., Phase evolution and nucleus growth observation of solid-state BaTiO3powder prepared by high-energy bead milling for raw material mixing, Jpn. J. Appl. Phys. 50 (2011), https://doi.org/10.1143/JJAP.50.091502.

[42] M. Rössel, H.R. Höche, H.S. Leipner, D. Völtzke, H.P. Abicht, O. Hollricher, et al., Raman microscopic investigations of BaTiO3 precursors with core-shell structure, Anal. Bioanal. Chem. 380 (2004) 157–162, https://doi.org/10.1007/s00216-004-2712-0.

[43] J.R. Frade, M. Cable, Reexamination of the basic theoretical model, J. Am. Ceram. Soc. 75 (1992) 1949–1957, https://doi.org/10.1111/j.1151-2916.1992.tb07222.x.

[44] L. Favergeon, M. Pijolat, M. Soustelle, Surface nucleation and anisotropic growth models for solid-state reactions, Thermochim. Acta 654 (2017) 18–27, https://doi.org/10.1016/j.tca.2017.05.004.

[45] H. Tagawa, K. Igarashi, Reaction of strontium carbonate with anatase and rutile, J. Am. Ceram. Soc. 69 (1986) 310–314, https://doi.org/10.1111/j.1151-2916.1986.tb04737.x.

[46] S. Kumar, L. Messing, Metal organic resin derived barium titanate: I I, kinetics of BaTiO, formation, J. Am. Ceram. Soc. 77 (1994) 2940–2948.

[47] J.G. Pepin, Thermal Shock Resistant Multilayer Ceramic Capacitor Termination Compositions, (1994) EP0589242, patent.

[48] J.T. Muckerman, J.H. Skone, M. Ning, Y. Wasada-tsutsui, Toward the accurate calculation of p K a values in water and acetonitrile, Biochim. Biophys. Acta 1827 (2013) 882–891, https://doi.org/10.1016/j.bbabio.2013.03.011.

[49] A. Kütt, S. Selberg, I. Kaljurand, S. Tshepelevitsh, A. Heering, A. Darnell, et al., pKa values in organic chemistry–Making maximum use of the available data, Tetrahedron Lett. 59 (2018) 3738–3748, https://doi.org/10.1016/j.tetlet.2018.08.054.

[50] H.Z. Akbas, Z. Aydin, F. Guder, S. Turgut, Accelerated formation of BaTiO3ceramics with mechanochemical processing in different liquids, J. Alloy. Comp. 699 (2017) 87–91, https://doi.org/10.1016/j.jallcom.2016.12.369.

[51] M.T. Buscaglia, M. Bassoli, V. Buscaglia, R. Alessio, Solid-state synthesis of ultrafine

BaTiO3 powders from nanocrystalline BaCO3 and TiO2, J. Am. Ceram. Soc. 88 (2005) 2374–2379, https://doi.org/10.1111/j.1551-2916.2005.00451.x.
[52] D.F.K. Hennings, B.S. Schreinemacher, H. Schreinemacher, Solid-state preparation of BaTiO $_3$ -based dielectrics, using ultrafine raw materials, J. Am. Ceram. Soc. 84 (2001) 2777–2782, https://doi.org/10.1111/j.1151-2916.2001.tb01094.x.
[53] S. Tashiro, K. Ishii, Phase change in calcination process for BaTi2O5and proposal of a new temperature profile, Adv. Powder Technol. 25 (2014) 761–766, https://doi.org/10.1016/j.apt.2013.11.007.
[54] K.R. Kambale, A.R. Kulkarni, N. Venkataramani, Grain growth kinetics of barium titanate synthesized using conventional solid state reaction route, Ceram. Int. 40 (2014) 667–673, https://doi.org/10.1016/j.ceramint.2013.06.053.
[55] U. Manzoor, D.K. Kim, Synthesis of nano-sized barium titanate powder by solid-state reaction between barium carbonate and titania, J. Mater. Sci. Technol. 23 (2007) 655–658.
[56] C.Y. Chang, C.Y. Huang, Y.C. Wu, C.Y. Su, C.L. Huang, Synthesis of submicron BaTiO3 particles by modified solid-state reaction method, J. Alloy. Comp. 495 (2010) 108–112, https://doi.org/10.1016/j.jallcom.2010.01.096.
[57] M.T. Buscaglia, M. Bassoli, V. Buscaglia, R. Vormberg, Solid-state synthesis of nanocrystalline BaTiO3: reaction kinetics and powder properties, J. Am. Ceram. Soc. 91 (2008) 2862–2869, https://doi.org/10.1111/j.1551-2916.2008.02576.x.
[58] T. Badapanda, V. Senthil, D.K. Rana, S. Panigrahi, Relaxor ferroelectric behavior of “A” site deficient Bismuth doped Barium Titanate ceramic, J. Electroceram. 29 (2012) 117–124, https://doi.org/10.1007/s10832-012-9754-z.
[59] T.M. Stawski, S.A. Veldhuis, O.F. Göbel, J.E. Ten Elshof, D.H.A. Blank, Effects of reaction medium on the phase synthesis and particle size evolution of BaTiO3, J. Am. Ceram. Soc. 93 (2010) 3443–3448, https://doi.org/10.1111/j.1551-2916.2010.03827.x.
[60] R. Yanagawa, M. Senna, C. Ando, H. Chazono, H. Kishi, Preparation of 200 nm BaTiO3 particles with their tetragonality 1.010 via a solid-state reaction preceded by agglomeration-free mechanical activation, J. Am. Ceram. Soc. 90 (2007) 809–814, https://doi.org/10.1111/j.1551-2916.2007.01498.x.
[61] G. Philippot, C. Elissalde, M. Maglione, C. Aymonier, Supercritical fluid technology: a reliable process for high quality BaTiO3based nanomaterials, Adv. Powder Technol. 25 (2014) 1415–1429, https://doi.org/10.1016/j.apt.2014.02.016.
[62] M.A. Bollinger, M.A. Vannice, A kinetic and DRIFTS study of low-temperature carbon monoxide oxidation over Au—TiO2 catalysts, Appl. Catal. B Environ. 8 (1996) 417–443, https://doi.org/10.1016/0926-3373(96)90129-0.
[63] W. Xu, D. Raftery, J.S. Francisco, Effect of irradiation sources and oxygen concentration on the photocatalytic oxidation of 2-propanol and acetone studied by in situ FTIR, J. Phys. Chem. B 107 (2003) 4537–4544, https://doi.org/10.1021/jp025995h.
[64] C.-C. Li, J.-H. Jean, Dissolution and dispersion behavior of barium carbonate in aqueous suspensions, J. Am. Ceram. Soc. 85 (2004) 2977–2983, https://doi.org/10.1111/j.1151-2916.2002.tb00566.x.
[65] H. S, T. Stephen, Solubilities of Inorganic and Organic Compounds, (1964) Elmsford, New York 10523, U.S.A..
[66] L. Bin Xiong, J.L. Li, B. Yang, Y. Yu, Ti 3+ in the surface of titanium dioxide: generation, properties and photocatalytic application, J. Nanomater. 2012 (2012), https://doi.org/10.1155/2012/831524.
[67] H. Abicht, D. Vo, A. Ro, F. Chemie, F. Physik, The influence of the milling liquid on the properties of barium titanate powders and ceramics, J. Mater. Chem. 7 (1997) 487–492.
[68] M. Del Arco, S. Gutiérrez, C. Martín, V. Rives, FTIR study of isopropanol reactivity on calcined layered double hydroxides, Phys. Chem. Chem. Phys. 3 (2001) 119–126, https://doi.org/10.1039/b007282f.
[69] S.A. Fuente, C.A. Ferretti, N.F. Domancich, V.K. Díez, C.R. Apesteguía, J.I. Di Cosimo, et al., Adsorption of 2-propanol on MgO surface: a combined experimental and theoretical study, Appl. Surf. Sci. 327 (2015) 268–276, https://doi.org/10.1016/j.apsusc.2014.11.159.
[70] G.S. Foo, F. Polo-Garzon, V. Fung, D.E. Jiang, S.H. Overbury, Z. Wu, Acid-Base Reactivity of Perovskite Catalysts Probed via Conversion of 2-Propanol over Titanates and Zirconates, (2017), https://doi.org/10.1021/acscatal.7b00783.
[71] G. Litwinienko, G.A. Dilabio, P. Mulder, H. Korth, K.U. Ingold, Intramolecular and intermolecular hydrogen bond formation by some ortho-substituted Phenols : some surprising results from an experimental and theoretical investigation, J. Phys. Chem. A 113 (2009) 6275–6288.
[72] R.N. Moussawi, D. Patra, Modification of nanostructured ZnO surfaces with curcumin: fluorescence-based sensing for arsenic and improving arsenic removal by ZnO, RSC Adv. 6 (2016) 17256–17268, https://doi.org/10.1039/c5ra20221c.
[73] K. Hadjiivanov, Identification and Characterization of Surface Hydroxyl Groups by Infrared Spectroscopy, first ed., Elsevier Inc., 2014, https://doi.org/10.1016/B978-0-12-800127-1.00002-3.
[74] G. Martra, Lewis acid and base sites at the surface of microcrystalline TiO2 anatase: relationships between surface morphology and chemical behaviour, Appl. Catal. Gen. 200 (2000) 275–285, https://doi.org/10.1016/S0926-860X(00)00641-4.
[75] C. Martín, I. Martín, V. Rives, B. Grzybowska, I. Gressel, A FTIR spectroscopy study of isopropanol reactivity on alkali-metal-doped MoO3/TiO2catalysts, Spectrochim. Acta Part A Mol. Spectrosc. 52 (1996) 733–740, https://doi.org/10.1016/0584-8539(96)01665-0.
[76] W. Xu, D. Raftery, Photocatalytic oxidation of 2-propanol on TiO2 powder and TiO2 monolayer catalysts studied by solid-state NMR, J. Phys. Chem. B 105 (2001) 4343–4349, https://doi.org/10.1021/jp004381e.
[77] G.S. Foo, F. Polo-Garzon, V. Fung, D.E. Jiang, S.H. Overbury, Z. Wu, Acid-base reactivity of perovskite catalysts probed via conversion of 2-propanol over titanates and zirconates, ACS Catal. 7 (2017) 4423–4434, https://doi.org/10.1021/acscatal.7b00783.
[78] J. Schneider, M. Matsuoka, M. Takeuchi, J. Zhang, Y. Horiuchi, M. Anpo, et al., Understanding TiO2photocatalysis: mechanisms and materials, Chem. Rev. 114 (2014) 9919–9986, https://doi.org/10.1021/cr5001892.
[79] I. Doroshenko, V. Pogorelov, V. Sablinskas, Infrared absorption spectra of monohydric alcohols, Dataset Pap. Chem. 2013 (2013) 1–6, https://doi.org/10.7167/2013/329406.
[80] G. S, H.H.H.D. Lutz, W. Eckers, Raman and infrared spectra of barium and strontium hydroxides and hydroxide hydrates, Spectrochim. Acta, Part A 37 (1981) 561–567.
[81] P.J.P.P.N. Trikalitis, Catalytic activity and selectivity of perovskites La1-xSrxV3 + V4 + 03 for the transformation of isopropanol, Appl. Catal. Gen. 131 (1995) 309–322.
[82] E. Farfan-Arribas, R.J. Madix, Role of defects in the adsorption of aliphatic alcohols on the TiO2(110) surface, J. Phys. Chem. B 106 (2002) 10680–10692, https://doi.org/10.1021/jp020729p.
[83] D. Brinkley, T. Engel, Photocatalytic dehydrogenation of 2-propanol on TiO 2 ( 110 ), J. Phys. Chem. B 1022 (1998) 7596–7605, https://doi.org/10.1021/jp9819011.
[84] U.-Y. Hwang, H.-S. Park, K.-K. Koo, Behavior of barium acetate and titanium isopropoxide during the formation of crystalline barium titanate, Ind. Eng. Chem. Res. 43 (2004) 728–734, https://doi.org/10.1021/ie030276q.
[85] M. Bensitel, V. Moraver, J. Lamotte, O. Saur, J.C. Lavalley, Infrared study of alcohols adsorption on zirconium oxide: reactivity of alkoxy species towards CO2, Spectrochim. Acta Part A Mol. Spectrosc. 43 (1987) 1487–1491, https://doi.org/10.1016/S0584-8539(87)80035-1.
[86] G.A.M. Hussein, N. Sheppard, M.I. Zaki, R.B. Fahim, Infrared spectroscopic studies of the reactions of alcohols over group IVB metal oxide catalysts. Part 3.-Ethanol over TiO2, ZrO2 and HfO2, and general conclusions from parts 1 to 3, J. Chem. Soc. Faraday. Trans. 87 (1991) 2661–2668, https://doi.org/10.1039/FT9918702661.
[87] G. Marcì, E. García-López, L. Palmisano, Photo-assisted degradation of 2-propanol in gas-solid regime by using TiO2impregnated with heteropolyacid H3PW12O40, Catal. Today 144 (2009) 42–47, https://doi.org/10.1016/j.cattod.2008.11.010.
[88] P. Galhotra, J.G. Navea, S.C. Larsen, V.H. Grassian, Carbon dioxide (C16O2 and C18O 2) adsorption in zeolite y materials: effect of cation, adsorbed water and particle size, Energy Environ. Sci. 2 (2009) 401–409, https://doi.org/10.1039/b814908a.
[89] F. Boccuzzi, S. Tsubota, M. Haruta, Vibrational investigation of CO adsorbed on gold deposited on TiO2, J. Electron. Spectrosc. Relat. Phenom. 64–65 (1993) 241–250, https://doi.org/10.1016/0368-2048(93)80085-Z.
[90] F.X. Llabrés i Xamena, A. Zecchina, FTIR spectroscopy of carbon dioxide adsorbed on sodium- and magnesium-exchanged ETS-10 molecular sieves, Phys. Chem. Chem. Phys. 4 (2002) 1978–1982, https://doi.org/10.1039/b110483g.
[91] E. Garrone, B. Bonelli, C. Lamberti, B. Civalleri, M. Rocchia, P. Roy, et al., Coupling of framework modes and adsorbate vibrations for CO2molecularly adsorbed on alkali ZSM-5 zeolites: mid- and far-infrared spectroscopy and ab initio modeling, J. Chem. Phys. 117 (2002) 10274–10282, https://doi.org/10.1063/1.1519254.
[92] B.H. Bui, R.S. Zhu, M.C. Lin, Thermal decomposition of iso-propanol: first-principles prediction of total and product-branching rate constants, J. Chem. Phys. 117 (2002) 11188–11195, https://doi.org/10.1063/1.1522718.
[93] F. Arsac, * D. Bianchi, J.M. Chovelon, C. Ferronato, J.M. Herrmann, F. Arsac, et al., Experimental microkinetic approach of the photocatalytic oxidation of isopropyl alcohol on TiO2. Part 1. Surface elementary steps involving gaseous and adsorbed C3HxO species, J. Phys. Chem. A 110 (2006) 4202–4212, https://doi.org/10.1021/JP055342B.
[94] J. Baltrusaitis, J.H. Jensen, V.H. Grassian, FTIR spectroscopy combined with isotope labeling and quantum chemical calculations to investigate adsorbed bicarbonate formation following reaction of carbon dioxide with surface hydroxyl groups on Fe 2 O 3 and Al 2 O 3, J. Phys. Chem. B 110 (2006) 12005–12016.
[95] R. Ashiri, Analysis and characterization of phase evolution of nanosized BaTiO 3 powder synthesized through a chemically modified sol-gel process, Met. Mater. Trans. A 43 (2012) 4414–4426, https://doi.org/10.1007/s11661-012-1242-1.
[96] D.W. Smith, An acidity scale for binary oxides, J. Chem. Educ. 64 (1982) 480–481, https://doi.org/10.1021/ed064p480.
[97] S.G. Bratsch, Electronegativity and the acid-base character of binary oxides, J. Chem. Educ. 65 (1988) 877–878, https://doi.org/10.1021/ed065p877.
[98] J.N. Kuhn, U.S. Ozkan, Surface properties of Sr- and Co-doped LaFeO3, J. Catal. 253 (2008) 200–211, https://doi.org/10.1016/j.jcat.2007.10.005.
[99] M.M. Natile, E. Ugel, C. Maccato, A. Glisenti, LaCoO3: effect of synthesis conditions on properties and reactivity, Appl. Catal. B Environ. 72 (2007) 351–362, https://doi.org/10.1016/j.apcatb.2006.11.011.